A Novel Model of Delamination Bridging
via Z-pins in Composite Laminates

G. Allegri[*], M. Yasaee, I.K. Partridge and S.R. Hallett
Advanced Composites Centre for Innovation and Science (ACCIS)
University of Bristol, Queen's Building
BS8 1TR, Bristol, UK

Abstract

A new micro-mechanical model is proposed for describing the bridging actions exerted by through-thickness reinforcement on delaminations in prepreg based composite materials, subjected to a mixed-mode (I-II) loading regime. The model applies to micro-fasteners in the form of brittle fibrous rods (Z-pins) inserted in the through-thickness direction of composite laminates. These are described as Euler-Bernoulli beams inserted in an elastic foundation that represents the embedding composite laminate. Equilibrium equations that relate the delamination opening/sliding displacements to the bridging forces exerted by the Z-pins on the interlaminar crack edges are derived. The Z-pin failure meso-mechanics is explained in terms of the laminate architecture and the delamination mode. The apparent fracture toughness of Z-pinned laminates is obtained from as energy dissipated by the pull out of the through-thickness reinforcement, normalised with respect to a reference area. The model is validated by means of experimental data obtained for single carbon/BMI Z-pins inserted in a quasi-isotropic laminate.

Keywords

A. Composite Materials; B. Fibre Reinforced; C. Delamination; D. Toughness;

[*] Corresponding author
e-mail: giuliano.allegri@bristol.ac.uk
Tel: +44 (0) 117 3315329
FAX: +44(0) 117 927 2771

Nomenclature

α	: insertion asymmetry (Eq. 1)
A	: cross-sectional area of the Z-pin
$\overline{\beta}$	: relative stiffness constant (Eq. 12)
D	: Z-pin diameter
δ	: total displacement during pull out tests (Eq. 39)
E	: Young's modulus of the Z-pin material in the axial direction
d	: normalised pull out displacement (Eq. 2)
f	: enhancement coefficient for the residual frictional force (Eq. 9)
ϕ	: mode-mixity coefficient (Eq. 3)
G_{LT}	: longitudinal-transversal shear stiffness for the Z-pin material
G^{*}	: apparent delamination toughness of Z-pinned laminate (Eq. 35)
G_{IC}^{f}	: fracture toughness for the tensile fibre failure of a single Z-pin
I	: second moment of area of the Z-pin cross-section
I_{s}	: second moment of area of the Z-pin cross-section with longitudinal splits
κ	: shear correction factor in Timoshenko's beam theory
k_{x}^{-}, k_{x}^{+}	: foundation stiffness for the lower and upper sub-laminates (Eq. 8)
L	: Z-pin overall length
L^{-}, L^{+}	: insertion lengths in lower and upper sub-laminates (Fig. 8)
m	: Weibull's exponent
M	: resultant bending moment along the Zpin
$\overline{M}$	: bridging bending moment (Eq. 32)
λ	: ratio of second moments of area for the split/pristine configuration
μ	: Coulomb's friction coefficient
N	: resultant normal force along the Z-pin
n	: normalised resultant normal force along the Z-pin (Eq. 10)
ν_{LT}	: longitudinal-transversal Poisson's ratio for the Z-pin material
ξ	: normalised abscissa along the Z-pin axis (Eq. 10)
p	: distributed axial force along the Z-pin

p^-, p^+	: distributed axial forces in the lower and upper sub-laminates (Eq. 9)
p_0, p_1	: residual frictional forces per unit length (Eq. 9)
P	: total applied load during pull out tests (Eq. 38)
P_F	: failure probability according to Weibull's criterion (Eq. B.9)
$\bar{\pi}^-$, $\bar{\pi}^+$	: normalised residual frictional forces along the Z-pin axis (Eqs. 14, 19)
q	: distributed transversal force along the Z-pin
q^-, q^+	: distributed transversal forces in the lower and upper sub-laminates (Eq. 7)
ρ	: areal density of Z-pins (Eq. 34)
σ	: normal stress in the Z-pin cross section
σ_{max}	: maximum normal stress in the Z-pin cross section
σ_s	: scaling constant for Weibull's failure probability (Eq. 26)
$\bar{\sigma}_{max}$	: Z-pin strength from Weibull's criterion (Eq. 27)
τ	: maximum shear stress in the Z-pin cross section
θ	: rotation of the Z-pin cross-section (Eq. A.6)
T	: resultant shear force along the Z-pin (Eq. A.8)
τ_{max}	: maximum cross-sectional shear stress (Eq. 40)
u	: transversal displacement of the Z-pin
U	: delamination sliding displacement at Z-pin location
V_0, V_{eff}	: reference volume and effective volume for Weibull's failure criterion (Eq. B.6)
W	: delamination opening displacement at the Z-pin location
x	: abscissa on transversal axis
X_T	: tensile strength according to ASTM D3039
$\bar{X}$	: shear bridging force (Eq. 32)
y	: normalised transversal displacement (Eq. 10)
Y	: normalised delamination sliding displacement (Eq. 10)
Ψ	: energy dissipated via bridging (Eq. 33)
z	: abscissa on longitudinal axis
$\bar{Z}$	: axial bridging force (Eq. 36)
ω	: tension to bending ratio (Eq. B.1)

1. Introduction

1.1 Literature Review

Through-thickness reinforcement has proved an effective means for inhibiting delamination growth in fibre-reinforced laminated composites [17]. It can be applied in the form of sub-millimetre diameter rods, tufts or stitches.

The through-thickness insertion of solid rods into an uncured laminate is commonly denoted as Z-pinning [24]. The rods can be either metallic or composite [8]. The insertion is usually performed with an ultrasonic gun [18, 24]. The Z-pins can be selectively inserted in areas prone to delamination. Several authors have carried out extensive experimental work for assessing the damage tolerance capability of Z-pinned composites. Single Z-pin pull out tests have also been performed in order to characterise the individual Z-pin response under mode I, II and mixed-mode loading [6-7, 35-36]. The increase in the apparent fracture toughness due to Z-pinning has been demonstrated using standard double cantilever beam (DCB), mixed-mode bending (MMB) and end-notch flexure (ENF) coupons [3, 6, 10-11, 26, 30-31]. Z-pinning has also been shown to improve the damage tolerance of composite lap-joints and T-joints [1-3, 9, 21], subjected to static and fatigue loading. Moreover, it has been demonstrated that Z-pinning augments the low-velocity impact performance of both monolithic and sandwich laminates [38]. However, in Z-pinned composites, there exists a significant trade-off between the reduction of in-plane stiffness and strength and the improved delamination tolerance [25].

Large scale interlaminar crack bridging [12, 22] is the basic mechanism that allows the through-thickness reinforcement to inhibit delamination growth. Whilst most of the existing literature is focussed on stiches and on Z-pins, it is becoming recognised that the nature of the bridging action is strongly dependent on the specific kind of through-thickness reinforcement, the laminate architecture and the delamination mode.

Massabò [23] demonstrated how through-thickness reinforcement can induce a transition from mode I delamination opening to mode II sliding. In this case, large-scale bridging prevents the propagation of interlaminar cracks and the final failure is due to ply micro-buckling. The occurrence of large-scale bridging and local buckling failure poses severe limitations on the applicability of linear elastic fracture mechanics (LEFM) for modelling progressive delamination in through-thickness reinforced laminates. Ratcliffe and O'Brien [28] employed an empirical bi-linear bridging law to predict the mechanical response of Z-pinned DCB specimens. Cartié et al [6-7] considered Z-pinned ASTM coupons and T-joints. They derived an empirical pull out law from single Z-pin tests and represented the through-thickness reinforcement in FE analyses via a distributed nonlinear springs on the delaminated interface. Yan et al. [35-36] adopted a similar approach, using the J-integral to compute the energy release rate at the bridged delamination tip.

Cox [13-14] developed an analytical micro-mechanical model for a through-thickness tow subjected to mixed-mode loading. The tow was assumed to behave as a linear-elastic/perfect-plastic body, while the embedding laminate was described as a perfectly plastic medium. The constitutive response of the through-thickness reinforcement was obtained in the form of non-linear implicit functions, relating the crack opening displacements to the bridging forces. Cox's model [13-14] allows a description of various through-thickness reinforcement architectures, including inclined tows, by simply changing the boundary conditions for the equilibrium equations. Grassi and Zhang [19] employed Cox's model to predict the response of Z-pinned DCB specimens via FE analyses. Allegri and Zhang [1-2] proposed a meso-mechanical model where individual through-thickness rods are considered as perfectly rigid and embedded in a Winkler's type elastic foundation. This model has been applied to the FE analysis of tee and cruciform joint configurations. Most recently Bianchi and Zhang [3-4] have developed a meso-mechanical constitutive model for individual Z-pins subjected to

mode II fracture. The embedded segment of the through-thickness reinforcement is modelled as an Euler-Bernoulli beam embedded in an elastic-plastic foundation.

1.2 Paper Overview

This paper presents a micro-mechanical model of individual Z-pins subjected to mixed-mode (I-II) loading. It summarises the results of a series of experiments on single Z-pin coupons [37], complemented with observations of the Z-pin in-situ morphology and failure mode. A new model of delamination bridging due to Z-pins is introduced, in which the Z-pins are described as Euler-Bernoulli beams undergoing small but finite rotations upon elastic deformation. The insertion of the Z-pins is assumed to be orthogonal to the delamination plane. The approach proposed in this paper is valid for a general mixed-mode regime and it includes the modes I and II as special cases. Expressions for the bridging forces exerted by Z-pins and for the apparent fracture toughness of Z-pinned laminates are derived. The paper also presents the calibration and validation of the aforementioned Z-pin model by means of the experimental data provided by Ref. [37].

2. Experimental Characterisation

This section summarises and complements the experimental evidence gathered by Yasaee et al. [37] regarding the morphology and the mechanical behaviour of single composite Z-pins, subjected to mixed-mode loading. The aim is to provide a rationale for the modelling framework later described in Sec. 3. The specimen configuration adopted in the tests in Ref. [37] is presented in Fig. 1. The specimens were built by laying up 64 plies of IM7/8552 fibre-reinforced carbon/epoxy, for a total thickness of 8.1 mm. The laminate was split into two symmetric blocks by inserting a 16μm release film, in order to prevent bonding of the through-thickness mid-plane interface during cure. The stacking sequences were respectively

$[90°/-45°/0°/45°]_{4s}$ for the lower block and $[0°/45°/90°/-45°]_{4s}$ for the upper sub-laminate. Fully cured T300/BMI Z-pins, having a diameter D of 0.28mm, were inserted orthogonally into the laminate. The mixed-mode tests were carried out using a custom-built loading jig, shown in Fig. 2. Diametral tension was applied to the coupons in order to simultaneously pull out and shear the Z-pins.

2.1 Z-pin morphology

Extensive X-ray computed tomography (CT) and Scanning Electron Microscope (SEM) investigations were carried out in order to assess the in-situ morphology of the Z-pin after insertion and cure [37]. CT revealed that, consistently with what has already been reported in the literature [24], the Z-pins are misaligned with respect to the nominal insertion direction. The average misalignment angle with respect to the through-thickness direction for the coupons considered here was 13°, with a standard deviation of 4°. Misalignment is due to the tip chamfering of commercially available Z-pins. Tip chamfering eases the standard ultrasound-assisted insertion but it also prevents from controlling the actual orientation of the inserted rod [6, 26]. A CT scan of a coupon containing a highly misaligned Z-pin is shown in Fig. 3; this specimen was not included in the tested batch. It is also worth observing that the Z-pin in Fig. 3 is bent, possibly due to the resin flow and consequent ply slippage during cure. Other characteristic defects associated with Z-pin are resin rich areas, i.e. "pockets" surrounding the through thickness rods, and crimping of the laminate plies [6, 24, 26]. These cannot be visualised in the CT scan image in Fig. 3 due to low contrast, but are evident in SEM micrographs [37]. The excess lengths of the Z-pin on the laminate surfaces are sheared away before curing [18, 24, 26]. This causes a permanent bending of the Z-pin heads and a residual indentation on the resin pockets that surround the Z-pins, as sketched in Fig. 4.a. Fig 4.b shows a micrograph of one of the coupons tested in Ref. [37], where both the bending of

the Z-pin head and the resin pocket indentation are evident. Asymmetric pull out of symmetrically inserted Z-pins has been extensively reported in the literature [6, 24, 26]. This can be explained by considering that one of the bent heads offers less "anchoring" than the other. When one of the bent tips is dragged into the laminate, an increase of friction may be observed. If the Z-pin is not fully inserted within the laminate, it is natural that the chamfered tip will tend to experience pull out [6, 26].

2.2 Z-pin failure

Three point bending tests have been carried out on individual T300/BMI Z-pins using the miniature rig shown in Fig. 5.a. These tests are not suitable for identifying the actual mechanical properties of Z-pins, since the rollers have too large a diameter compared to the Z-pin cross sectional radius. However, the tests provide a qualitative indication of the failure mode experienced by the Z-pin under combined bending and shearing. As shown in Fig. 5.a, the Z-pin ultimately breaks due to tensile fibre failure, with a characteristic "brooming" of carbon splinters. Splitting of the Z-pin, which is governed by the matrix shear strength, was observed well before ultimate failure without any significant loss of bending stiffness. Compressive failure did not occur at all. Tensile fibre failure is also observed in single Z-pin coupons under mixed-mode loading [37], as shown in Fig. 5.b.

For the T300/BMI Z-pins, Cartié et al [6, 8] reported a Young's modulus $E = 115$ GPa and a tensile strength of 1100 MPa. The strength value is well below what basic composite micro-mechanics would suggest for a composite with a 57% volumetric fraction of T300 fibre. The typical strength of a unidirectional T300 composites tested in tension (ASTM D3039 [39]) is 1860 MPa [40] for a 57% fibre volume fraction. However, the volume of a single Z-pin is at least 2000 times smaller than that of an ASTM standard coupon and, according to the Weibull's failure criterion [5, 29, 34], the Z-pin tensile strength should be much higher than

the reported 1860 MPa. This discrepancy may be attributed to the difficulty of testing single Z-pins in tension, particularly in terms of avoiding stress concentrations at the loading grips.
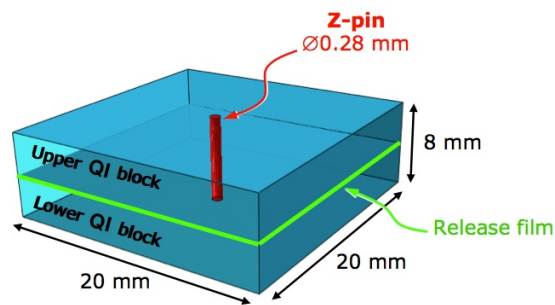

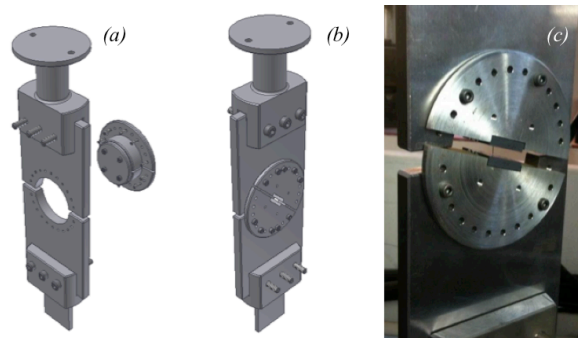Fig. 1. Coupons for single Z-pin testing.

Fig. 2. Mixed-mode fixture for single Z-pin testing; (a) back view; (b) front view; (c) assembled jig during a Z-pin pull out test.
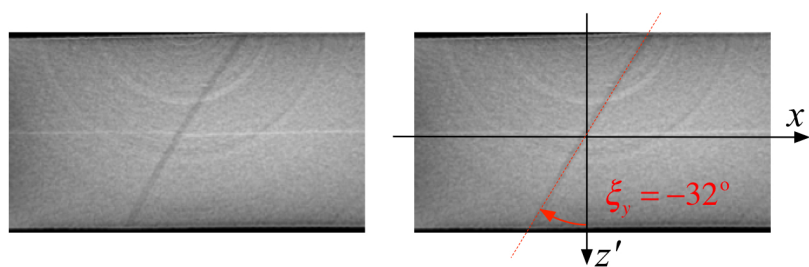

Fig. 3. CT scan image of a Z-pin and evaluation of the associated misalignment angle.

2.3 Mechanical response of a single Z-pin

In Ref. [37], the mechanical response of single Z-pin coupons was characterised by recording the load-displacement curves at a range of mode-mixities ϕ between 0 (mode I) and 1 (mode II). The mode-mixity was defined as the ratio of the delamination sliding displacement to the total displacement. Rotating of the loading jig shown in Fig. 2.c allowed varying the mode-mixity. All the experimental tests were performed in displacement-control. The nominal mode-mixity was corrected considering the actual Z-pin misalignment angle, obtained for each of the coupons tested via CT scans. The detailed procedure for calculating the actual test mode-mixity for misaligned Z-pins is described in Ref. [37].

Fig. 6 presents a plot of the apparent toughness G^* from the experimental tests on single Z-pin coupons as a function of the corrected mode-mixity ϕ [37].

In Fig. 6, the apparent toughness is calculated by computing the overall work spent to pull out the Z-pin, divided by a reference area associated to a nominal 2% aerial density of through-thickness reinforcement. Note that, due to the inherent misalignment of the Z-pins, it was not possible to test in pure mode I and mode II. The experimental data show an increase of the apparent toughness in single Z-pin coupons for mode-mixity values ranging from 0 to 0.4. In the aforementioned range, all the Z-pins experienced complete pull out during the tests. The enhancement of apparent fracture toughness with mode-mixity is due to Coulomb friction [14].
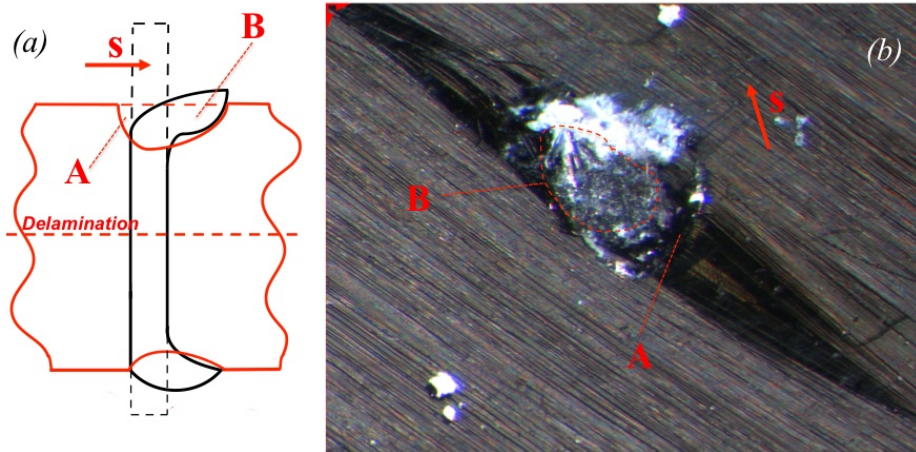
Fig. 4. Tip morphology of a fibrous Z-pin (Z-pin) after manufacturing: (a) sketch of the Z-pin configuration (tip deformation exaggerated); (b) top view of the Z-pin tip on the insertion side of a laminate, with the area (B) showing the bent Z-pin tip. The shearing direction for removing the excess length on the insertion side is denoted by *s*.
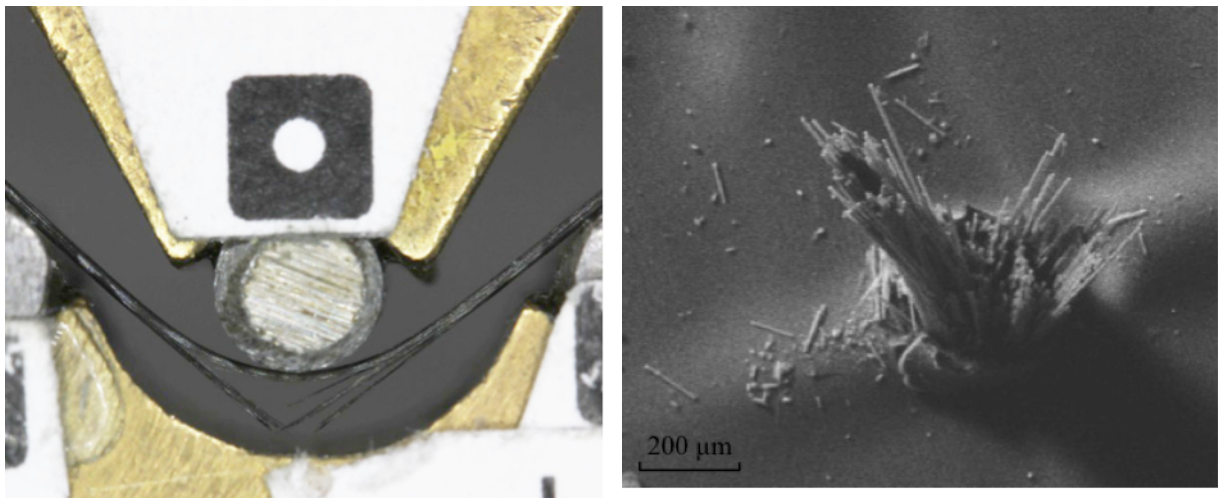

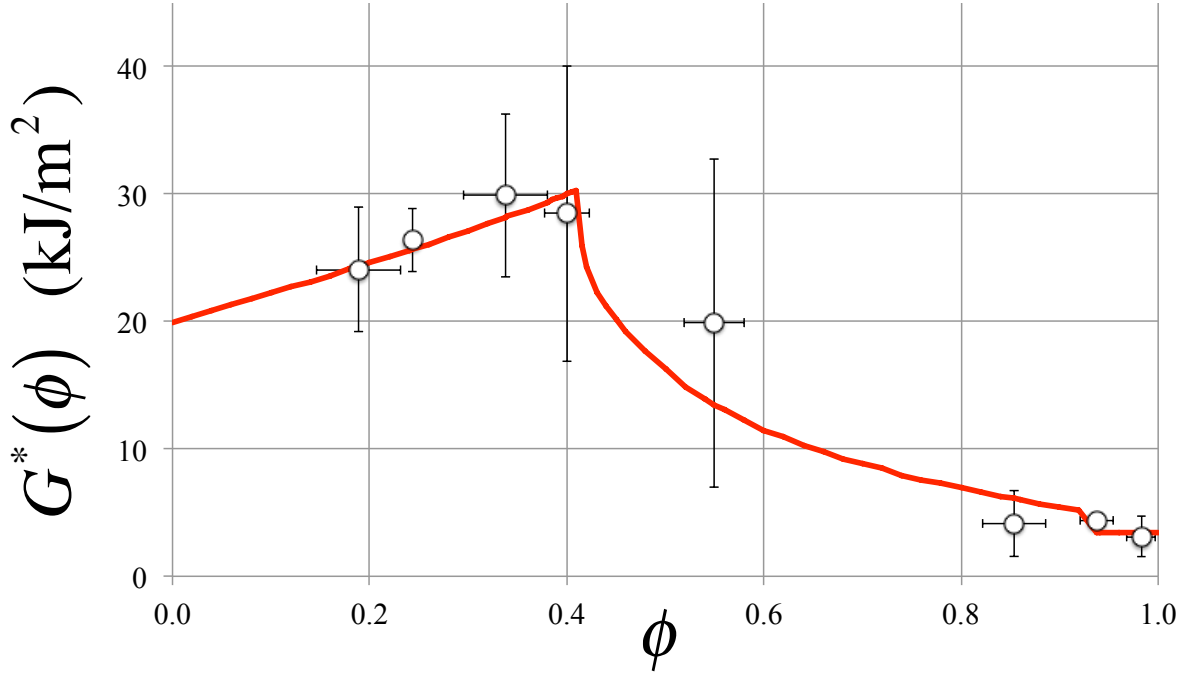Fig. 5. Failure mode of a single Z-pin; (a) three point bending test; (b) SEM image of a failed single Z-pin coupon.

Fig. 6. Apparent fracture toughness of single Z-pin coupons normalised for a 2% aerial density versus mode-mixity. Results from the calibrated model (Sec. 5) in red line.

In Fig. 6, for ϕ ranging from 0.4 to 0.8, there exists a "transition" region [37], where the Z-pin behaviour progressively switches from complete pull out to early failure. In other words, some of the tested Z-pins prematurely failed, while others still experienced full pull out. The associated apparent toughness steadily decreases with the mode-mixity. Finally, for $\phi > 0.8$, i.e. in a mode II dominated regime, all the Z-pins failed before pull out had been completed and the apparent toughness plateaued to a minimum.

Fig. 7a shows that the Z-pin response in a mode I dominated regime, i.e. $\phi = 0.189$, is characterised by two main stages. At first the force required to pull-put the Z-pin steadily grows. This suggests that the frictional forces exerted by the laminate on the Z-pin initially increase, as it has to be expected if one of the Z-pin bent tips is dragged into the laminate. Then the frictional forces reach a limit value and, consequently, the pull out progresses with a decreasing applied force, since the embedded length of the Z-pin gets shorter.
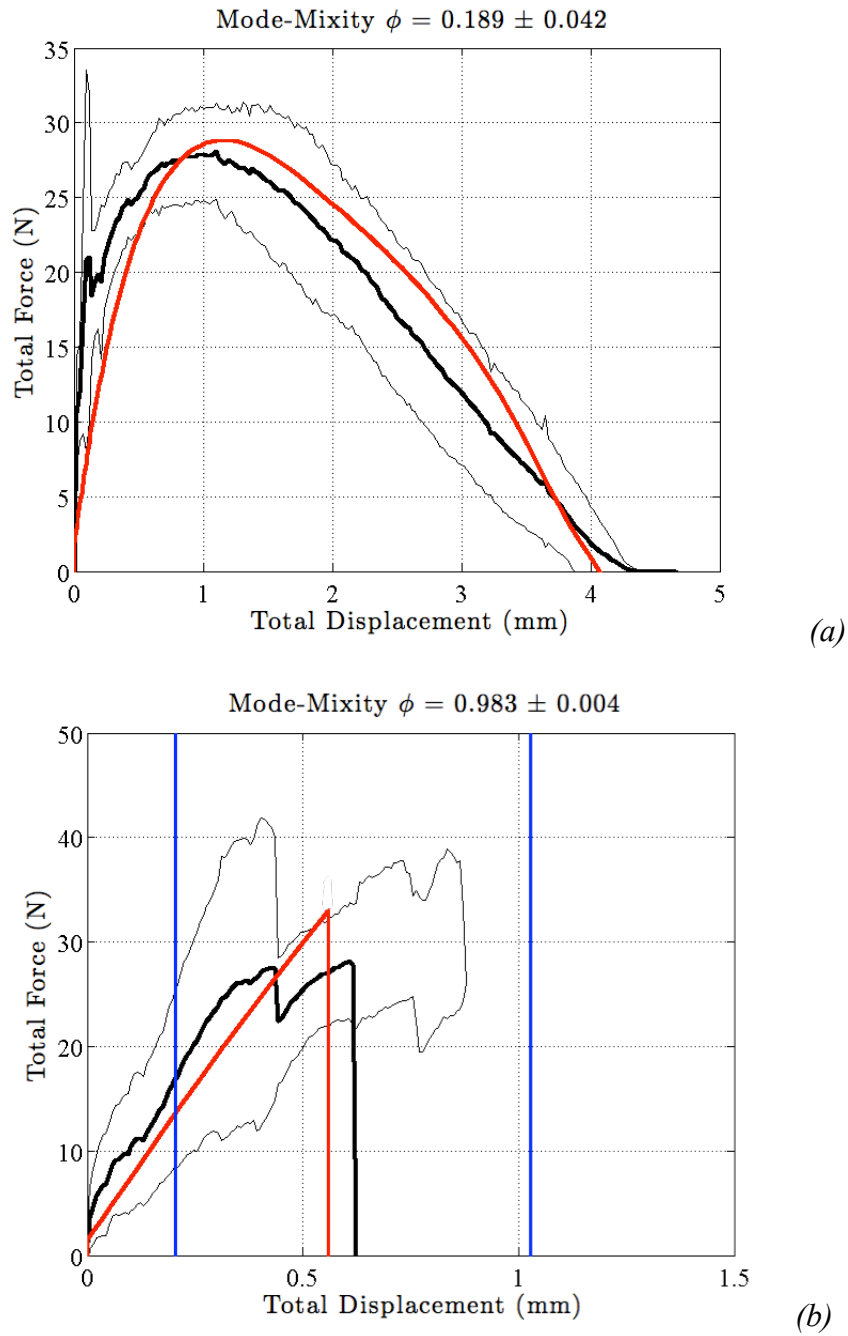
Fig. 7. Comparison of load-displacement plots for calibration; average experimental values [37] in thick black lines; results from the calibrated model (Sec. 5) in thick red lines. The thin black lines represent plus/minus one standard deviation from the mean experimental load. The blue vertical lines in (b) represent the bounds of plus/minus one standard deviation from the average displacement to failure.

Fig. 7b shows the Z-pin response in a mode II dominated regime, i.e. $\phi = 0.983$. For all the specimens tested in this case (8 in total), the load increased almost linearly with the sliding displacement, until sudden failure occurred in the pulled-out segment, close to the delamination surface.

The scatter of the experimental data presented in Figs. 6 and 7 is large. The apparent toughness values have a considerable coefficient of variation, particularly in the transition region, despite the fact that the nominal mode-mixity was corrected for the actual misalignment angle. This suggests that misalignment alone is not sufficient to explain the observed variability of the Z-pin behaviour. The Z-pin residual curvature shown in Fig. 3 and the defects due to the insertion, i.e. resin pockets and ply crimping, also play a major role in determining the mechanical response of the through-thickness reinforcement [24]. The residual curvature induces a pre-stress in the Z-pin, which influences its apparent strength under applied mechanical loading. The resin rich areas and local ply crimpling also affect the stress transfer from the laminate to the Z-pin. Overall, these defects represent inherent "features" of Z-pinned laminates. Characterising these features at single Z-pin level is not possible in structural applications, where thousands of Z-pins may be used. Therefore, the emphasis here is on establishing a modelling framework that allows representing the average trends of apparent fracture toughness and load-displacement response of single Z-pins.

3. Model Formulation

3.1 Problem statement

A Z-pin having a total length L is embedded into a composite laminate. A mixed-mode delamination propagates within the laminate and intersects the Z-pin at a known depth. The two sub-laminates split by the delamination are assumed to have the same elastic properties. The Z-pin counteracts the delamination opening/sliding displacements by exerting bridging

forces on the interlaminar crack surfaces. These forces are tangential and normal to the delamination plane. Considering the reference configuration in Fig. 8a, the delamination plane cuts the Z-pin in two segments, "lower" and "upper", having respectively length L^- and L^+; $L = L^- + L^+$ is the Z-pin total length. Without loss of generality, it is hereby assumed that pull out affects the lower embedded segment L^-. The following "insertion asymmetry" parameter (IAP) is introduced

$$\alpha = \frac{L^-}{L^- + L^+} \tag{1}$$

If a delamination intersects the Z-pin at half of the insertion length, i.e. in the case of symmetric insertion, one has $\alpha = 1/2$.

The opening displacement in the wake of the delamination tip is responsible for the Z-pin pull out, as shown in Fig. 8b. It is here assumed that the delamination opening is entirely accommodated by a "rigid" pull out displacement W, as shown in Fig. 8b. During pull out, the length of the "lower" embedded segment of the Z-pin is reduced to $L^- - W$. A normalized pull out displacement is thus defined as:

$$d = \frac{W}{L^-} \tag{2}$$

The sliding displacement of the delamination surface causes the Z-pin to shear and bend, as qualitatively illustrated in Fig. 8c. While deforming in the transverse direction relative to the laminate, the embedded Z-pin segments are supported by foundation forces exerted by the surrounding composite. Let U be the relative transversal displacement of the two sub-laminates surrounding the Z-pin; U is measured with respect to the Z-pin tips, as shown in Fig. 8c.

The mode-mixity ϕ at the Z-pin location is defined as the ratio of the sliding displacement to the total displacement [37], i.e.

$$\phi = \frac{U}{\sqrt{U^2 + W^2}} \tag{3}$$

The pull-out displacement U and the local mode-mixity ϕ are here considered as independent variables, with the exception of pure mode II. Consequently the overall sliding displacement is expressed as:

$$U = \frac{\phi}{\sqrt{1-\phi^2}} W \tag{4}$$

for $\phi < 1$. In the special case $\phi = 1$, i.e. for a local pure mode II regime, U must be considered as the independent variable since $W = 0$.

3.2 Equilibrium equations for a single Z-pin

The Z-pin is modelled as an Euler-Bernoulli beam subjected to small but finite rotations. Therefore, the equilibrium equations for an infinitesimal segment of the Z-pin can be stated in the following form:

$$EI\frac{d^4u}{dz^4} - N\frac{d^2u}{dz^2} + q = 0 \tag{5}$$

$$\frac{dN}{dz} = -EI\frac{d^3u}{dz^3}\frac{d^2u}{dz^2} - p \tag{6}$$

Eqs. (5-6) are derived in Appendix A. In Eqs. (5-6), E is the Z-pin Young's modulus and I is the cross-sectional second moment of area; u is the transversal elastic displacement of the Z-pin, directed along the x axis in Fig. 8a. N represents the resultant axial force on the Z-pin cross-section; p and q are distributed loads per unit length, respectively collinear and normal to the Z-pin longitudinal axis z. The distributed loads represent the frictional and foundation forces exerted on the Z-pin by the embedding laminate. The bending moment M and cross-sectional shear force T associated with Eqs. (5-6) are given in Eqs. (A.7-8).

3.3 Foundation and Frictional Forces

We consider three different types of distributed forces acting on the Z-pin in a mixed-mode regime, namely: 1) Winkler's foundation forces; 2) "residual" frictional forces; 3) Coulomb frictional forces. In the following discussion, $[...]^-$ and $[...]^+$ respectively indicate quantities evaluated within the lower and the upper embedded segments.

A Winkler's foundation provides a support force whose magnitude is proportional to the relative displacement between the Z-pin and the surrounding laminate and opposite in direction.
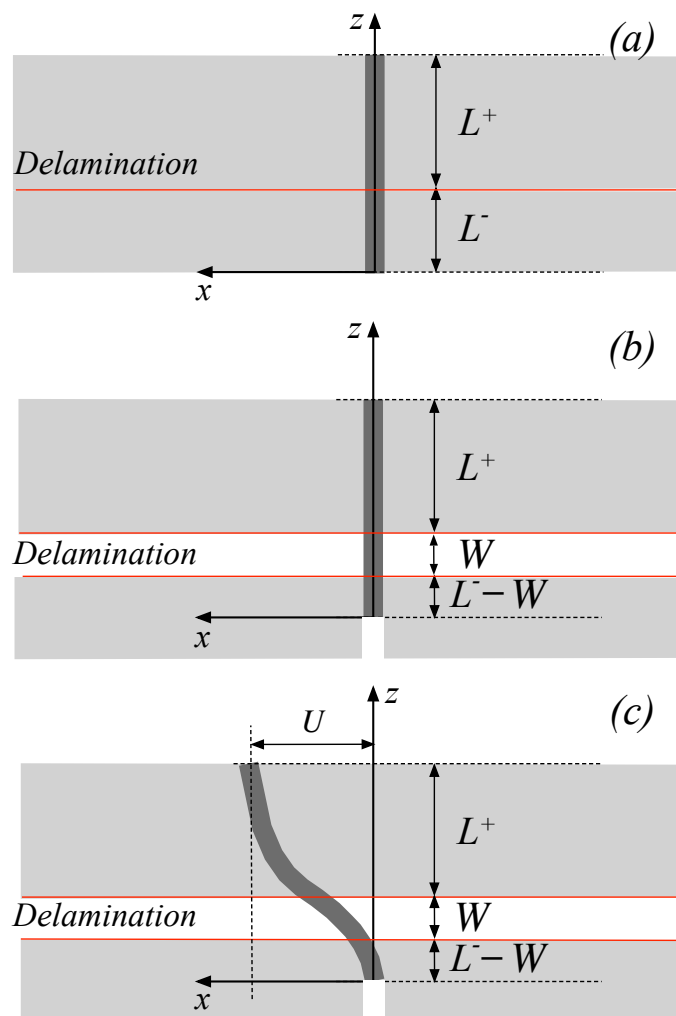

Fig. 8. Assumed bridging kinematics of the Z-pin; (a) reference configuration; (b) opening mode; (c) sliding mode.

By virtue of the sign conventions adopted in Appendix A, one can therefore write

$$q^- = k^- u, \qquad q^+ = k^+ (u - U) \qquad (7)$$

where k_x^- and k_x^+ are foundation stiffness constants associated with the lower and upper sub-laminates in Fig. 8. In principle, the foundation stiffness constants depends on the ply elastic constants and laminate stacking sequence, as well as on the Z-pin elastic properties and diameter. In a quasi-isotropic laminate k_x^- and k_x^+ should be independent of the direction of the transverse displacement, i.e. the foundation itself should be quasi-isotropic. In the literature, the assumption of Winkler's foundation has been already employed for the analysis of single Z-pin behaviour [1-4]. Here, since it has been assumed that the lower and upper sub-laminates have the same elastic properties, one has:

$$k_x^- = k_x^+ = \overline{k}_x \qquad (8)$$

where $\overline{k}_x$ is the foundation stiffness value for both the sub-laminates.

Thermal residual stresses on the Z-pin lateral surface are compressive [24]. These induce a residual friction, which is usually modelled as a tangential load per unit length. The latter is usually assumed independent from the pull out displacement W [2, 6, 8, 13-14]. In practise, depending on the Z-pin tip morphology, the residual friction may vary during pull out, as discussed in Sec. 2.1. In a mixed-mode regime, the Coulomb friction associated with the transversal foundation forces in Eq. (7) will increase the distributed tangential load [14]. Therefore, the tangential forces acting on the Z-pin are assumed as follows:

$$p^- = -p_0 - (p_1 - p_0)e^{-fW} - \mu k_x^- |u| \qquad p^+ = p_1 + \mu k_x^+ |U - u| \qquad (9)$$

where μ is the coefficient of Coulomb friction; p_0 and p_1 are residual frictional forces per unit length; f is a positive scaling constant, whose unit is an inverse length. If $p_0 = p_1$, Eq. (9) leads to the constant residual friction scenario already discussed in the literature [2, 6,

8, 13-14]. However, assuming $p_0 > p_1$ it is possible to account for an increase of residual friction during pull out, while for $p_0 < p_1$ the residual friction decreases.

3.4 Equilibrium equations for the lower embedded Z-pin segment

The following normalized variables are here defined respectively for the axial abscissa z, the transverse displacement u, the normal force N and the relative displacement U of the Z-pin tips

$$\xi = \frac{z}{L} \qquad y = \frac{u}{D} \qquad n = \frac{NL^2}{EI} \qquad Y = \frac{U}{D} \tag{10}$$

By substituting the first of Eqs. (7) into Eq. (5) and rearranging the latter in terms of the normalized variables defined in Eq. (10), the following differential equation is obtained for the normalized transverse displacement

$$y^{IV} - ny'' + 4\overline{\beta}^4 y = 0 \tag{11}$$

Where the constant $\overline{\beta}$ is defined as:

$$\overline{\beta} = \frac{L}{\sqrt{2}} \sqrt[4]{\frac{\overline{k_x}}{EI}} \tag{12}$$

Similarly, substituting the first of Eqs. (7) and the first of Eqs. (9) into the axial equilibrium equation (6) and switching to the normalized variables from Eq. (10), the non-linear differential equation governing the distribution of the normalized axial force n in the lower embedded segment is sought

$$n' = -\left(\frac{D}{L}\right)^2 y'' y''' + 4\overline{\beta}^4 \left[\overline{\pi}^-(d) + \mu\left(\frac{D}{L}\right)|y| \right] \tag{13}$$

where

$$\overline{\pi}^-(d) = \frac{p_0 + (p_1 - p_0)e^{-\alpha f dL}}{\overline{k_x} L} \tag{14}$$

Let us assume that the Z-pins are moderately slender, i.e.

$$\left(\frac{D}{L}\right)^2 \ll 1 \tag{15}$$

Thus Eq. (13) can be approximated as follows:

$$n^I = +4\overline{\beta}^4\left[\overline{\pi}^-(d) + \mu\left(\frac{D}{L}\right)|y|\right] \tag{16}$$

3.5 Equilibrium equations for the upper embedded Z-pin segment

Considering the normalized variables defined in Eq. (10) and substituting the second of Eqs. (7) and the second of Eqs. into Eq. (5) yields the following differential equation for the transverse displacement of the upper embedded segment of the Z-pin

$$y^{IV} - ny^{II} + 4\overline{\beta}^4(Y - y) = 0 \tag{17}$$

where the constant $\overline{\beta}$ is the same given by Eq. (15). Similarly, substituting the second of Eqs. (7) and the second of Eqs. (9) into Eq. (6) and considering the normalized variables in Eq. (10) yield the non-linear differential equation ruling the normalized axial force n in the upper embedded segment

$$n^I = -\left(\frac{D}{L}\right)^2 y^{II}y^{III} - 4\overline{\beta}^4\left[\overline{\pi}^+(d) + \mu\left(\frac{D}{L}\right)|Y - y|\right] \tag{18}$$

where

$$\overline{\pi}^+ = \frac{p_1}{k_x L} \tag{19}$$

Therefore, for moderately slender Z-pins, i.e. if the condition stated in Eq. (15) holds, Eq. (22) can be approximated as follows

$$n^I = -4\overline{\beta}^4\left[\overline{\pi}^+(d) + \mu\left(\frac{D}{L}\right)|Y - y|\right] \tag{20}$$

20

3.6 Assembled governing equations

The pulled-out portion of the Z-pin, defined by $L^- - W < z < L^-$, is free from the action of the lateral normal and tangential distributed forces, so $p = q = 0$ for $L^- - W < z < L^-$.

Taking advantage of the definitions in Eqs. (3) and (10), the normalized total transversal displacement is obtained as a function of the nominal mode-mixity

$$Y = \frac{\alpha \phi d}{\sqrt{1 - \phi^2}} \left(\frac{L}{D} \right) \tag{21}$$

Considering Eqs. (11), (16-17), (20-21), the governing equations for the normalized transverse displacement y and axial force n can now be recast in the following non-linear ordinary differential system

$$y^{IV} - n y^{II} = \begin{cases} -4\bar{\beta}^4 y, & 0 \le \xi \le \alpha(1-d) \\ 0, & \alpha(1-d) < \xi < \alpha \\ -4\bar{\beta}^4 \left[y - \frac{\alpha \phi d}{\sqrt{1-\phi^2}} \left(\frac{L}{D} \right) \right], & \alpha \le \xi \le 1 \end{cases} \tag{22.a}$$

$$n^I = \begin{cases} 4\bar{\beta}^4 \left[\bar{\pi}^-(d) + \mu \left(\frac{D}{L} \right) |y| \right] & 0 \le \xi \le \alpha(1-d) \\ 0, & \alpha(1-d) < \xi < \alpha \\ 4\bar{\beta}^4 \left[\bar{\pi}^+ + \mu \left(\frac{D}{L} \right) \left| y - \frac{\alpha \phi d}{\sqrt{1-\phi^2}} \left(\frac{L}{D} \right) \right| \right], & \alpha \le \xi \le 1 \end{cases} \tag{22.b}$$

Continuity conditions are imposed for the transverse displacement, rotation, bending moment, shear force and axial force at the interfaces between the lower embedded segment, the pulled out portion and the upper embedded segment.

3.7 Boundary Conditions

Regarding the geometric boundary conditions, the relative transverse displacement at the lower embedded segment root of the Z-pin is here set to zero. On the other hand, the transverse displacement at the tip of the upper embedded segment must be equal to U, as shown in Fig. 8. Therefore in terms of normalized variables one has

$$y(0)=0 \qquad y(1)=\frac{\alpha\phi d}{\sqrt{1-\phi^2}}\left(\frac{L}{D}\right) \tag{23}$$

Moreover, we assume that the bent head of the Z-pin constraints the rotation, i.e.

$$y^I(1)=0 \tag{24}$$

Eq. (24) represents an idealization of the actual case, since the bent Z-pin head will have a finite compliance, albeit the latter is difficult to estimate due to the significant variability in the configuration of the sheared-off tips.

In terms of natural boundary condition, the axial force and bending moment are set to zero at the tip of the lower embedded segment, since the latter is free to translate and rotate during pull out. Thus one has:

$$n^I(0)=y^{II}(0)=0 \tag{25}$$

The differential system of equations (22) must be solved with the boundary condition in Eqs. (23-25) for each pull out displacement $W \in \left[0, L^-\right]$ and mode-mixity coefficient $\phi \in \left[0,1\right)$. For $\phi=1$, i.e. the pure mode II case, there is no pull out displacement, so the overall transverse displacement U must be imposed directly as a geometric boundary condition. However, the pull out may not take place completely, since the through-thickness Z-pin may experience failure for $W = W^*(\phi) < L^-$, or, equivalently, for $d = d^*(\phi) < 1$, where the asterisk denotes the rupture condition of the through-thickness rod.

3.8 Failure criterion for brittle fibrous Z-pin

According to the Weibull's criterion [20, 29, 34], the probability of failure for a solid having volume V and subjected to a stress field $\sigma(x,y,z)$ is given by

$$P_F = \begin{cases} 1 - e^{-\int_V \left[\frac{\sigma(x,y,z)}{\sigma_s}\right]^m dV}, & \sigma(x,y,z) > 0 \\ 0, & \sigma(x,y,z) \leq 0 \end{cases} \tag{26}$$

where $\sigma(x,y,z)$ is the stress within the solid, m is the Weibull's modulus and σ_s is a scaling constant. As demonstrated in Appendix B, for a Z-pin subjected to a distribution of axial force $N(z)$ and bending moment $M(z)$, failure occurs when

$$\overline{\sigma}_{\max} = X_T \left[\frac{V_0}{V_{eff}}\right]^{\frac{1}{m}} \tag{27}$$

where $\overline{\sigma}_{\max}$ is the average peak tensile stress along the Z-pin axis. In Eq. (27), X_T is the average is fibre failure strength associated to a volume of material V_0 subjected to pure tension, while V_{eff} is the effective volume of the Z-pin subjected to variable tension and bending. The expressions of the effective volume V_{eff} and the average peak tensile stress $\overline{\sigma}_{\max}$ for a beam having circular cross-section are given respectively in Eqs. (B.6) and (B.7).

3.9 Remarks on the modelling assumptions

3.9.1 Mode mixity-definition

The mode-mixity definition in Eqs. (3-4) is strictly valid for an orthogonally inserted Z-pin. As discussed in Sec. 2, the Z-pins are affected by some misalignment. Although in the model the pin is assumed to be orthogonal to the delamination plane, in the model calibration and validation (Sec. 5) the frame of reference of the loading is rotated to account for the pin initial misalignment. This correction procedure adopted is the same described in Ref. [37], where it

was introduced in order to factor out the effect of the initial misalignment from the experimental data. The correction is legitimate if the Z-pin misalignment angles are small, otherwise the laminate foundation stiffness may be significantly affected.

3.9.2 Euler-Bernoulli beam hypothesis

Adopting an Euler-Bernoulli beam model implies neglecting the cross-sectional shear deformation of the Z-pin. It is worth investigating the validity of this assumption in a quantitative fashion. A more refined approach to modelling the Z-pin response would be represented by the adoption of Timoshenko's beam theory [33]. It is well known that Timoshenko's theory reverts to the Euler-Bernoulli beam theory if the following condition is met:

$$\frac{EI}{\kappa L^2 A G_{LT}} << 1 \tag{28}$$

where κ is the shear correction factor and G_{LT} is the material longitudinal-transversal shear stiffness. The condition stated in Eq. (28) is valid also for a beam embedded in an elastic foundation, as demonstrated in Appendix C. Considering the expression of the area and the second moment of area for circular cross-section, Eq.(28) can be rearranged as:

$$\left(\frac{D}{L}\right)^2 << \frac{16kG_{LT}}{E} \tag{29}$$

The shear correction factor for a circular cross-section is given by [33]

$$\kappa = \frac{6(1+v_{LT})}{7+6v_{LT}} \tag{30}$$

where v_{LT} is the longitudinal-transversal Poisson's ratio. Considering G_{LT} = 5GPa and v_{LT} = 0.3 as representative values for the elastic properties of the T300/BMI Z-pin, Eq. (29) yields the following condition:

$$\left(\frac{D}{L}\right)^2 << 0.617 \qquad (31)$$

The reader can observe that the assumption of moderately slender Z-pin given Eq. (15) implies that the condition in Eq. (31) is satisfied, so, in principle, the Euler-Bernoulli hypothesis is valid. For the Z-pin configuration in Ref. [37], the left hand side of Eq. (31) is in fact 500 times less than the right hand side.

However, it must be noted that G_{LT} is a matrix-dominated property. If the matrix is elastic and brittle, as in the case of the BMI resin used in the Z-pins considered here, G_{LT} will be constant, the Euler-Bernoulli assumption is appropriate. On the other hand, if a matrix is ductile, G_{LT} will drop in the post-yield regime.

Given the Z-pin configuration considered here, even a 20-fold drop of G_{LT} would not impact the validity of the Euler-Bernoulli assumption. However, this also implies that the condition in Eq. (28) should be checked in order for the model to be applied to different Z-pin diameter, insertion length and constituents. If Eq. (28) does not hold (e.g. in the limit case of a perfectly plastic matrix behaviour, for which composite micro-mechanics dictates that $G_{LT} = 0$), then the Cox and Sridhar's model in Ref. [14] must be adopted, since it is based on the assumption that the shear response of a through-thickness tow is perfectly plastic. The latter hypothesis is clearly most appropriate for metallic Z-pins at high sliding displacement, whilst this paper is focussed on brittle composite through-thickness reinforcement, for which sliding displacements are small, as shown in Fig. 7.b.

3.9.3 Elastic foundation hypothesis

The elastic foundation assumption summarised in Eq. (7) is valid for small delamination sliding displacements. From tests performed on metallic Z-pins in polycarbonate and carbon Z-pins in unidirectional laminates [8], it was observed that through-thickness tows can

actually plough across the laminate, thus withstanding large sliding. This scenario is well described by assuming that the foundation is perfectly plastic as in Refs. [13-14]. However, unidirectional laminates have limited practical applications. In a multi-axial laminate (e.g. in the case of the quasi-isotropic stacking sequence considered here) Z-pins are in a heavily constrained state, whereby fibres counteract the lateral displacements due to delamination sliding. In order to clarify this point, Fig. 9.a shows the typical arrangement of a Z-pin in a unidirectional laminate; the resin pocket surrounding the Z-pin is shaded in yellow and the in-plane misalignment of the laminate fibres is also shown. If the Z-pin is sheared in the direction parallel to the fibres, its lateral displacement will be counteracted only by the matrix, which will yield. However, for a quasi-isotropic arrangement as that shown in Fig. 9.b, a different scenario arises. The fibres belonging to the adjacent laminae will bridge the resin pockets for any given ply orientation. The fibres will react to the lateral pressure exerted by the Z-pin by carrying axial loads. Even if the matrix yields, the laminate response to the lateral displacement of the Z-pin will be dominated by the stiffness of the fibres, which behave in a linear elastic fashion up to failure and are much stronger than the matrix. Therefore, it is reasonable to assume that the resulting response of the foundation will be linear elastic. Fig. 10 shows an SEM image of a single Z-pin coupon failed in a mode II dominated regime ($\phi > 0.8$) from the experimental tests described in Sec. 2. There is no evidence of Z-pin ploughing across the laminate. Similarly, there is no evidence of plastic indentation of the laminate due to the lateral displacement of the Z-pin. Also, the Z-pin failure is brittle and fibre dominated. Thus the experimental evidence provides decisive support for the assumption of elastic foundation made in this paper. It is expected that an elastic foundation model will be generally adequate for multi-axial laminates made of structural grade fibre-reinforced composites, fabrics included, with typical fibre volume fractions in excess of 50%.

However, a plastic foundation model as that described in Ref. [14] represents a more appropriate choice for multi-axial laminates with low fibre volume fractions and/or compliant reinforcement fibres and for the aforementioned case of unidirectional composites.
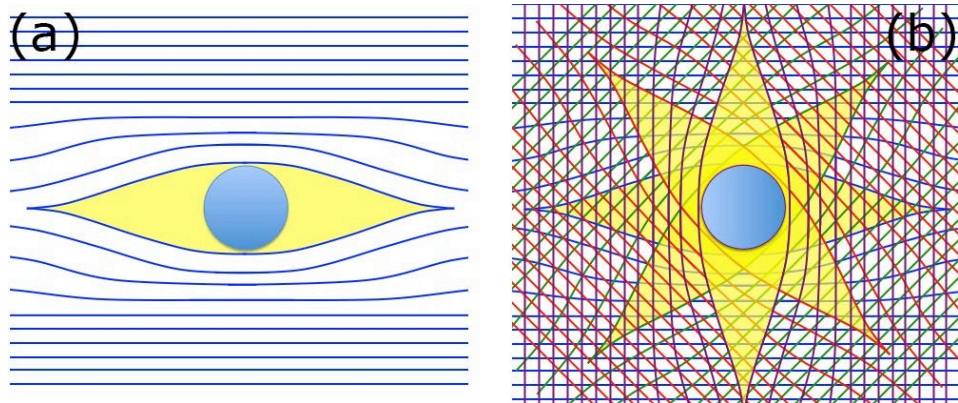

Fig. 9. Schematic architecture of the foundation arrangement for a Z-pin in:

a) a uni-directional laminate;

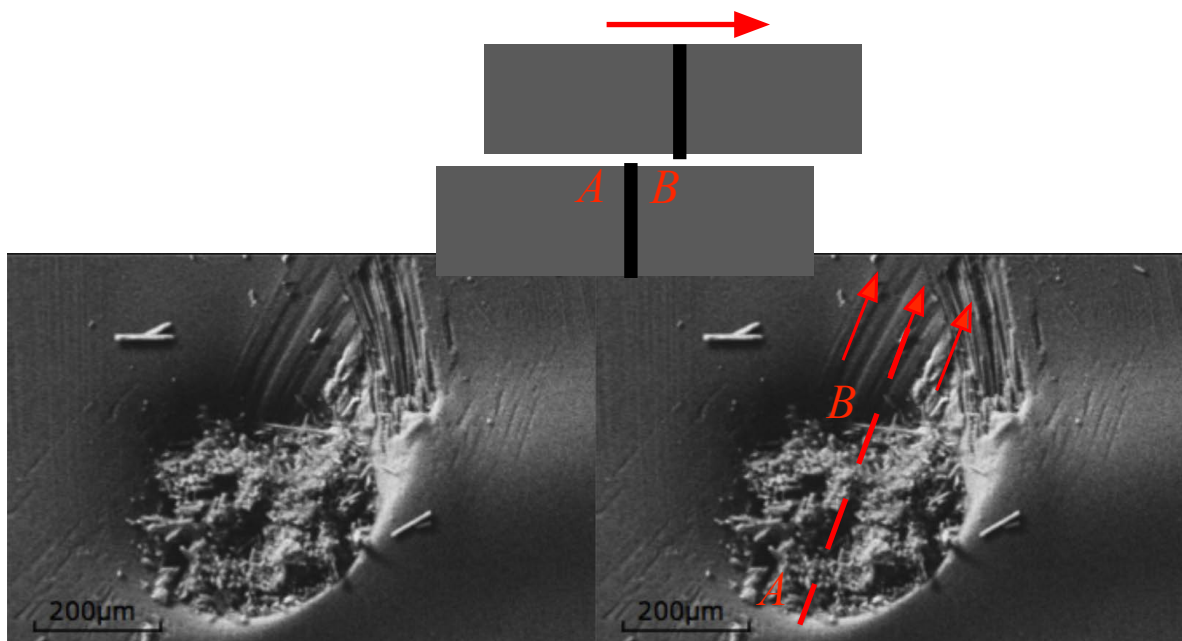b) a quasi isotropic laminate (0° ply in blue/45° ply in green/-45° ply in red/90° ply in purple).

Fig. 10. SEM image of Z-pin failed in pure mode II; the red arrows on the right give the shearing direction, visible from the scratch marks on the left.

4. Bridging Laws

4.1 Bridging forces
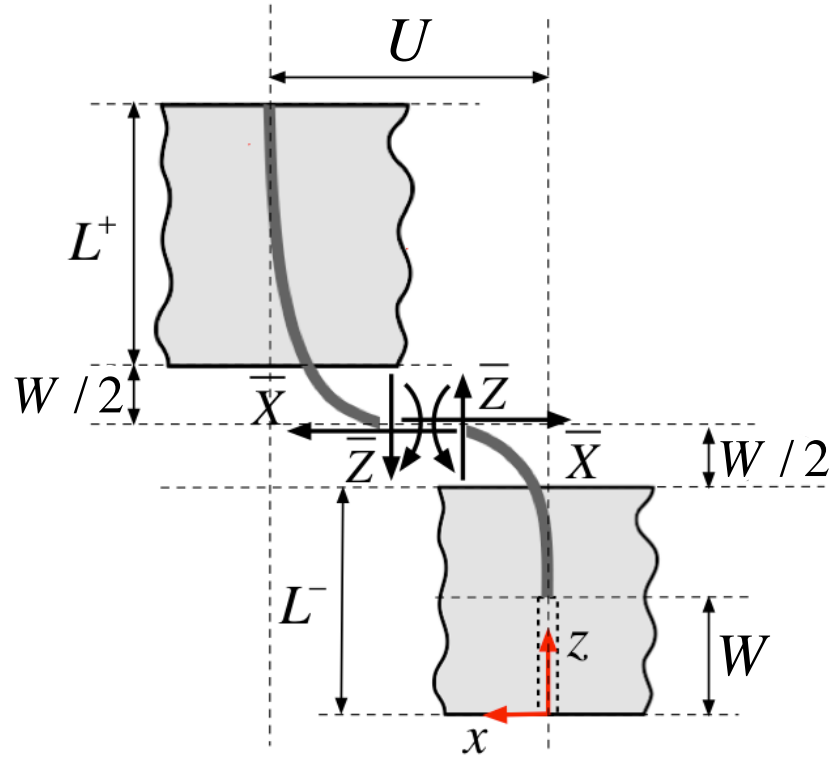
Fig. 11. Bridging forces and moment during Z-pin pull out; the labels of bending moments have been omitted for simplicity.

As shown in Fig. 11, the Z-pin bridging actions are represented by a force $\overline{X}$ directed along the x axis (i.e. parallel to the delamination surface), a through-thickness resultant $\overline{Z}$ (i.e. normal to the interlaminar crack plane) and a bending moment $\overline{M}$. These forces and moment are calculated at the mean delamination opening plane, i.e. for $z = \overline{z} := L^- - \dfrac{W}{2}$ or, equivalently, for $\xi = \overline{\xi} = \alpha\left(1 - \dfrac{d}{2}\right)$. The bridging forces here introduced can be represented by means of nonlinear springs or interface elements with custom traction/displacement laws in FE analysis [1-4, 6, 19, 35-36]. The bridging of the delamination edges occurs until the

normalised pull out displacement reaches the critical value $d = d^*(\phi)$, at which the Z-pin

failure occurs. Considering the projections of the beam cross-sectional resultants on the

coordinate axes z and x given in Eq. (A.12) and the normalized variables in Eq. (10), one

finds for $(D/L)^2 \ll 1$ and $0 \leq d < d^*(\phi)$:

$$\overline{Z}(d,\phi) = \frac{EI}{L^2} n \left\{ \alpha \left(1 - \frac{d}{2} \right) \right\}$$

$$\overline{X}(d,\phi) = \frac{EID}{L^3} \left\{ n \left[\alpha \left(1 - \frac{d}{2} \right) \right] y' \left[\alpha \left(1 - \frac{d}{2} \right) \right] - y''' \left[\alpha \left(1 - \frac{d}{2} \right) \right] \right\}$$

$$\overline{M}(d,\phi) = \frac{EID}{L^2} y'' \left[\alpha \left(1 - \frac{d}{2} \right) \right]$$

(32)

In Eq. (32), the dependency on the nominal local mode-mixity is implicit and it holds because

of the geometric boundary condition stated in the second of Eq. (23). Since a value of the

normalized sliding displacement Y in Eq. (21) can be associated to each combination of d and

ϕ, it is also possible to formulate the bridging forces given in Eq. (32) as implicit functions

of d and Y. Regarding the FE modelling of Z-pinning via interface elements, the implicit

dependency of the bridging forces on the delamination opening and sliding displacements

represents an additional issue. The latter may be circumvented by storing the bridging forces

as functions of the opening and sliding displacements in lookup tables, from which

interpolated values of $\overline{Z}(d,Y)$, $\overline{X}(d,Y)$ and $\overline{M}(d,Y)$ can be calculated during FE

simulations.

4.2 Energy absorbed via bridging

A Z-pin bridging a delamination allows dissipating mechanical energy via two fundamental

mechanisms: 1) the work done by frictional forces in Eq. (9), which arise during the

progressive pull out of the Z-pin from the surrounding laminate; 2) the energy which is

instantaneously spent to fracture the Z-pin at the normalized pull out displacement for failure $d = d^*(\phi)$. Denoting as Ψ the energy dissipated during the bridging process, we obtain

$$\Psi(\phi) = \alpha L \int_0^{d^*(\phi)} \overline{Z} \, \mathrm{d}d + \frac{\pi}{4} G_{IC}^f D^2 \tag{33}$$

where G_{IC}^f is the fibre-failure fracture toughness of the Z-pin. If complete pull out occurs, the second term on the right hand side of Eq. (33) disappears.

Let us consider a rectangular array of uniformly distributed Z-pins. The aerial density of the Z-pins in the array is defined as

$$\rho = \frac{\pi D^2}{4W^2} \tag{34}$$

where W is the length of the side of the unit cell associated to a single Z-pin [6]. The apparent fracture toughness $G^*(\phi)$ of a Z-pin array is here defined as the energy absorbed by bridging per unit delamination area. Thus, $G^*(\phi)$ can be calculated as the energy absorbed by a single Z-pin in the array divided by the unit cell, i.e.

$$G^*(\phi) = \frac{4\rho}{\pi D^2} \Psi(\phi) \tag{35}$$

From Eqs. (33-35), the mode II apparent fracture toughness for a laminate reinforced by fibrous brittle Z-pin is given by

$$G^*(1) = \rho G_{IC}^f \tag{36}$$

since no pull out occurs.

Eq. (36) proves that the apparent toughness in mode II depends only on the fracture toughness associated with the tensile fibre failure of the Z-pin and the aerial density of through-thickness reinforcement.

5. Model Calibration and Validation

5.1 Model implementation and calibration

The Z-pin model in Eqs. (22-25) has been implemented in MATLAB employing the built-in routine BVP4C that solves non-linear boundary value problems using an adaptive collocation method. The implementation is based upon discretising the normalised pull out displacement d and mode-mixity ϕ ranges. One hundred discretization points are considered in both cases. For each discretized value of d and ϕ the differential problem in in Eqs. (22-25) is solved, yielding the associated bridging forces in Eq. (32). At each mode-mixity ϕ, d is incremented until either the Z-pin fails according to the criterion in Eq. (27) or full pull out is achieved. Once either of the latter conditions is met, the mode-mixity value is incremented and the simulation repeated. Tab. 1 lists the Z-pin diameter D, total insertion length L and insertion asymmetry parameter α for the single Z-pin coupon in Fig. 1.

D (mm)	L (mm)	α
0.28	8	0.5

Table 1: Z-pin insertion parameters

Tab. 2 provides a list of the mechanical properties for the Z-pin stiffness, strength and friction. The reference strength X_T reported in Tab. 2 is that declared by the manufacturer of T300 fibres for a generic T300/epoxy system [40] with 57% fibre volume fraction. The tensile strength is a fibre dominated property and it is not expected to vary significantly when different matrix systems are employed. The strength was measured according to the ASTM D3039 standard [39]; the associated specimen volume V_0 is also reported in Tab. 2. The coefficient of friction $\mu = 0.7$ in Tab. 2 is that reported for HTA/6376 carbon/epoxy material

system [32]. A similar value of the friction coefficient, i.e. $\mu = 0.8$, has also been measured on pure BMI resin coupons [16].

E (GPa)	X_T (MPa)	V_0 (mm^3)	μ
115[a]	1860[b]	2250[c]	0.7[c]

[a] Refs. [6, 8]; [b] Ref. [40]; [c] Ref. [39]; [e] Ref. [16];

Table 2: Assumed stiffness, strength and friction properties for the Z-pin.

Considering the data in Tabs. 1 and 2, there are 6 remaining parameters that need to be estimated. These are the foundation stiffness $\bar{k}_x$, the parameters describing the residual friction (i.e. p_0, p_1 and f), the Weibull's exponent m and finally the fracture toughness of the tensile fibre failure G_{IC}^f. The 6 unknown parameters have been identified by means of a parallelized genetic algorithm (GA). The cost function to be minimized in the GA optimization is defined as follows

$$C = \sqrt{\varepsilon_{G^*(\phi)}^2 + \varepsilon_{P(\phi_1),\delta(\phi_1)}^2 + \varepsilon_{P(\phi_2),\delta(\phi_2)}^2} \tag{37}$$

In Eq. (37), $\varepsilon_{G^*(\phi)}^2$ is the relative mean square error of the apparent toughness obtained by Eq. (35) with respect to the experimental data. The reference aerial density value ρ has been assumed at 2%. Similarly $\varepsilon_{P(\phi_1),\delta(\phi_1)}^2$ and $\varepsilon_{P(\phi_2),\delta(\phi_2)}^2$ represent the mean square errors associated with the total load versus displacement curves obtained by the model with respect to the experimental data for the mode-mixity values $\phi_1 = 0.189$ and $\phi_2 = 0.983$. Note that in the model the total load applied P (Fig. 7) on the Z-pin is given by

$$P(d,\phi) = \sqrt{\bar{Z}^2(d,\phi) + \bar{X}^2(d,\phi)} \tag{38}$$

where $\overline{Z}(d,\phi)$ and $\overline{X}(d,\phi)$ are the bridging forces from Eq. (32). Similarly, by virtue of Eqs. (1), (2), (10) and (21), the total displacement δ (Fig. 7) is given by:

$$\delta(d,\phi) = \frac{\alpha dL}{\sqrt{1-\phi^2}} \tag{39}$$

The genetic algorithm optimization has been run on a population of 100 individuals. Convergence was achieved after approximately 110 generations. The calibration yields the parameters given in Tab. 3.

$\overline{k}_x$ (N/mm^2)	p_0 (N/mm)	p_1 (N/mm)	f (1/mm)	m	G_{IC}^f (kJ/m^2)
165	10.500	0.375	1.5	27	170

Table 3: Calibrated model parameters

Regarding the Weibull's exponent, large variations of m are reported in the literature depending on the material system and the loading regime considered. The Weibull's modulus typically ranges between 20 and 40, with most experimental values clustered around 30 [5, 33]. Thus the value yielded by the calibration procedure, i.e. $m = 27$ as given in Tab. 3, can be considered reasonable.

The value of fibre tensile fracture toughness G_{IC}^f obtained from the calibration and reported in Tab. 3 has the same order of magnitude of that measured on T300/epoxy composites, i.e. typically 130-150 kJ/m^2 [27].

Figs. 6 and 7 show that the results obtained from the calibrated model are within one standard deviation from the experimental data, both in terms of apparent fracture toughness and load-displacement response.

5.2 Model validation

Validation data are considered in Figs. 12a-f. These consist of 6 sets of load versus displacement curves for single Z-pin coupons obtained at mode-mixity values ranging from $\phi=0.243$ to $\phi=0.938$, which have not been included in the calibration set. The load-displacement curves predicted by the model have been obtained using the calibrated parameters given in Tab. 3. Figs. 12a-c present the load versus displacement curves up to a mode-mixity of $\phi=0.400$.
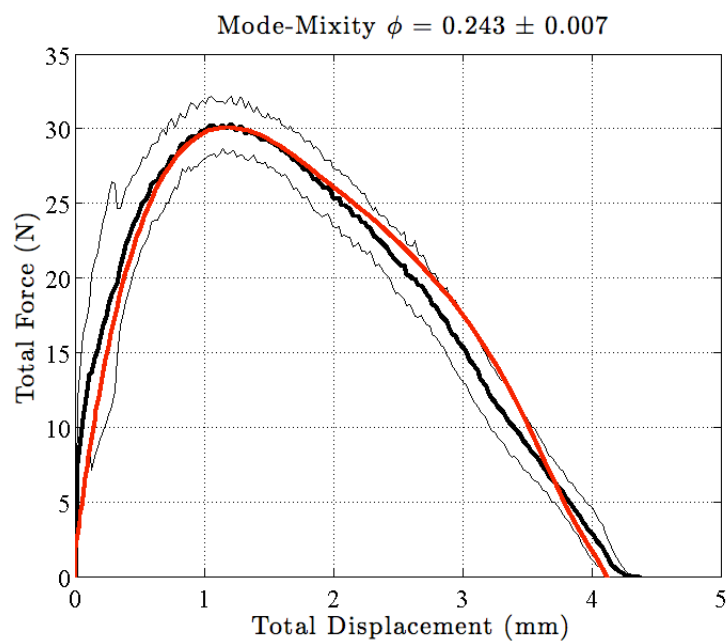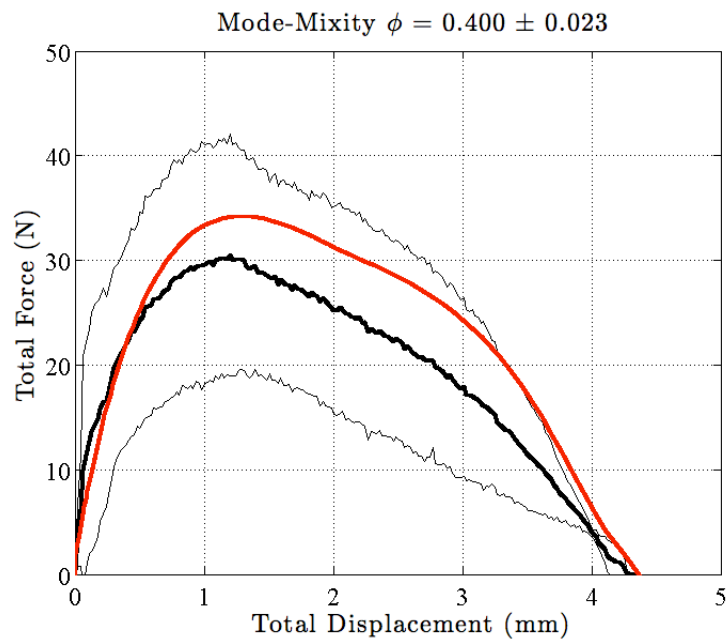

(a) 3 specimens tested

[Fig. 12; caption below]
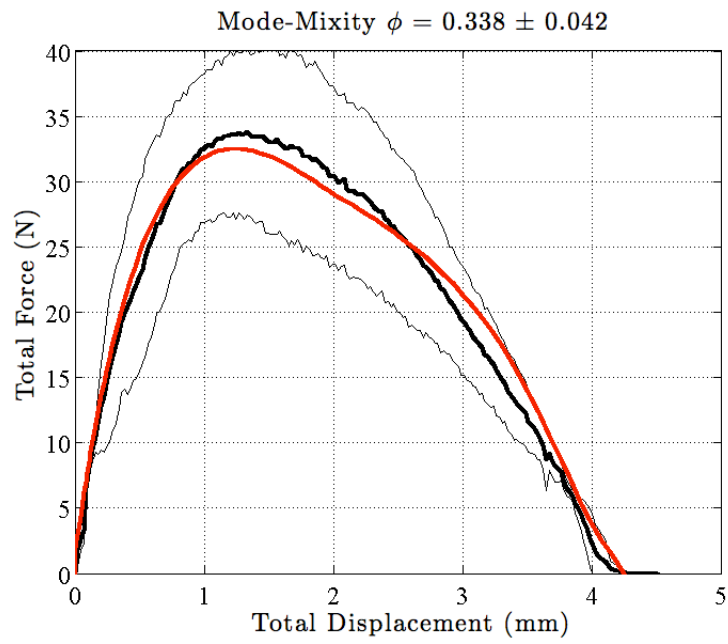
(b) 3 specimens tested

[Fig. 12; caption blow]

(c) 3 specimens tested; [Fig. 12; caption below]
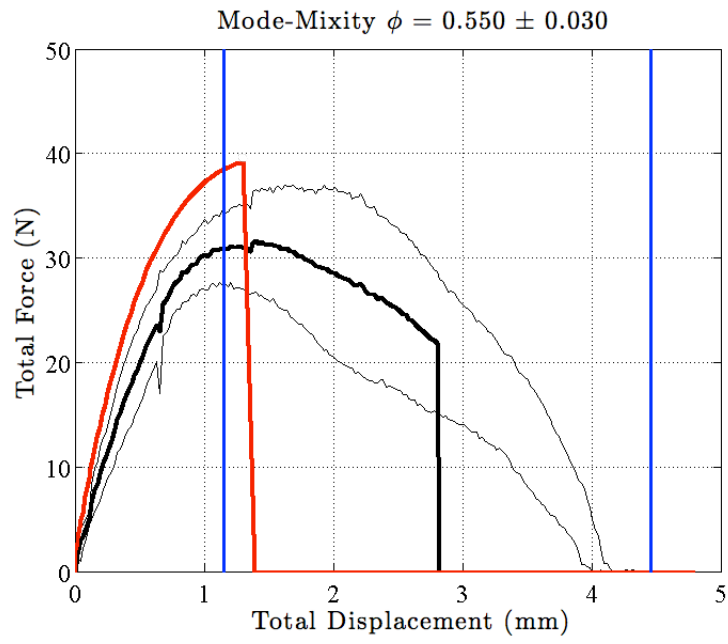
(d) 5 specimens tested; [Fig. 12; caption below]
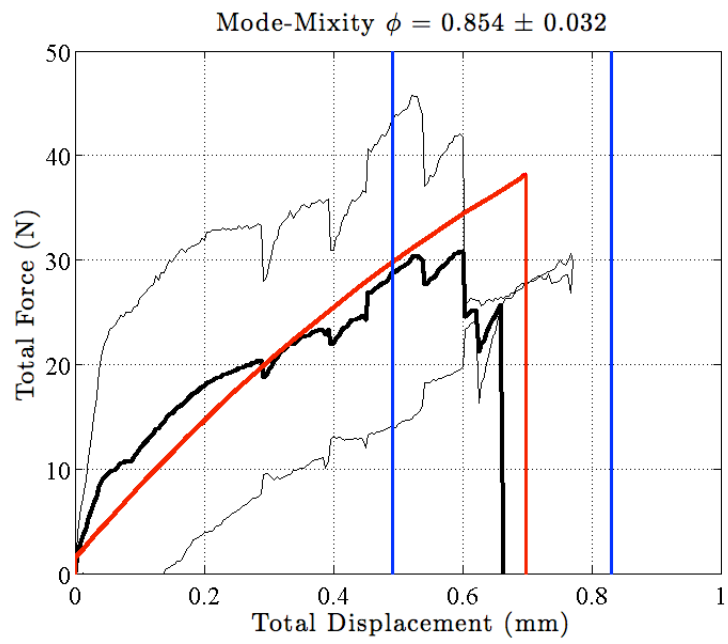
(e) 4 specimens tested; [Fig. 12; caption below]

Mode-Mixity $\phi = 0.938 \pm 0.017$
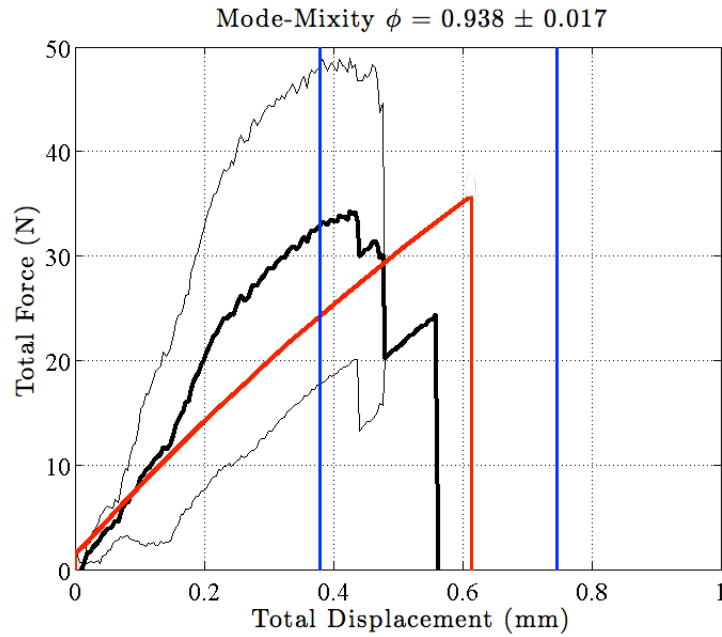
(f) 3 specimens tested

Fig. 12. Comparison of load-displacement plots for validation; average experimental values in thick black lines; model predictions in thick red lines. One standard deviation scatter bands on mean load in thin black lines. The blue vertical lines in (e-f) represent the bounds of plus/minus one standard deviation from the average displacement to failure.

For $\phi \leq 0.4$, all the Z-pin experienced complete pull out during the tests. There is an excellent agreement between the model prediction and the experimental results.

Fig. 12e-f shows two examples of the Z-pin response in mode II dominated regimes. All the Z-pin tested in these conditions failed before experiencing complete pull out. There is significant scatter in the experimental load-displacement curves and in the associated failure loads/displacements. However, the model predictions fall within the bounds of plus/minus standard deviation from the experimental averages.

A different scenario arises in Fig. 12.d, i.e. for a mode-mixity that falls in the transition region. For $\phi = 0.550$, 3 out of 5 Z-pins experienced full pull out, while 2 out of 5 failed prematurely. The deterministic model proposed here cannot capture this random failure

behaviour, which is due to the sources of uncertainty discussed in Sec 2.3. Consequently, as shown in Fig. 12.d, the predicted displacement to failure is significantly lower than the average one, while the peak force is overestimated with respect to the experimental data. Nonetheless, the apparent toughness value estimated by the model at $\phi = 0.550$ is still within one standard deviation from the experimental mean, as it can be observed in Fig. 1. In mode II, the Coulomb term in Eq. (11) causes a significant enhancement of the frictional force per unit length; considering the case of $\phi = 0.983$, the Coulomb terms is 90 times larger than the residual friction in the neighbourhood of the delamination surfaces at the failure displacement.

5.3 Analysis of the Z-pin failure mode

The Weibull's failure criterion in Eq. (30) is essentially nonlocal, i.e. failure may in principle occur anywhere within the body volume. Nonetheless, the probability of failure taking place in relatively low stressed regions is usually small enough to be neglected. Moreover, if significant stress concentrations arise within the body volume, the Weibull's criterion would predict that failure is localised in these highly stressed areas [20].

The sequence of pull out and failure for a single Z-pin coupon tested at $\phi = 0.550$ is presented in Fig. 13, showing that the Z-pin is being dragged out of the sub-laminate "C". The video frame in Figs. 13.a-b is the last before the sudden load drop associated with failure, while the image in Fig. 13.c is the first frame after failure. The red arrow in Fig. 13.a highlights the position of the Z-pin. The pull out displacement in Fig. 13.a-b is approximately 1.2 mm; at a mode-mixity of $\phi = 0.550$, the associated sliding displacement is 0.8 mm (Eq. 4). Hence the angle between the Z-pin and the through thickness direction should be $\tan^{-1}(0.8/1.2) \cong 33.7^O$. The actual orientation angle of the Z-pin is measured in Fig. 13.b and found to be approximately 35°, thus in good agreement with that dictated by the mode-mixity

value. Clearly this is not the "zero-load" misalignment angle of the Z-pin, since the orientation shown in Fig. 13.a-b is a consequence of the applied pull out and sliding displacements. The actual misalignment angle for the coupon shown in Fig. 13.a-b had been measured from CT scans and found to be approximately 5°. As already mentioned in Sec. 2.3, all the mode-mixity values reported in this paper have been corrected in order to account for the "zero-load" misalignment of the Z-pin, which was measured via CT scans for all the coupons [37]. From Fig. 13.c, it is observed that failure occurred on Z-pin half-length that is being pulled out from "C". The failure location is very close to the lower delamination surface, i.e. the surface of sub-laminate "C". The failure appears to take place within the laminate. This occurred consistently for all the mixed-mode specimens that failed by Z-pin fracture. At the highest mode-mixity values considered, i.e. $\phi = 0.938$ and $\phi = 0.983$, the pull out displacement is negligible and the failure is again located within the laminate and very close to the delamination plane. Fig. 13.c also shows the characteristic "brooming" of the Z-pin failed end. This is again a clear indication of tensile fibre failure.
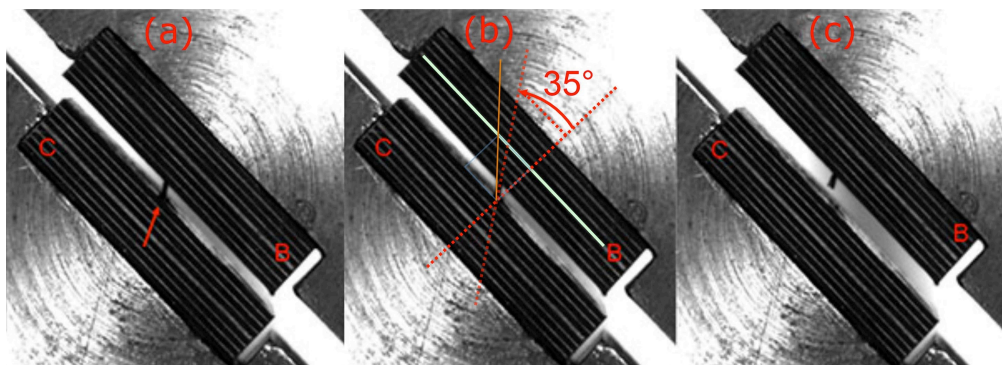

Fig. 13. Sequence of Z-Pin pull out and failure at $\phi = 0.550$; (a) Z-pin arrangement at a pull out displacement of 1.2 mm; (b) measured orientation angle of the Z-pin during mixed-mode pull out; (c) Z-pin failure.

The stress distribution in the Z-pin predicted by the model at the pull out failure displacement, $\eta = 1.23\,\text{mm}$, is presented in Fig. 14; σ_{max} is the maximum tensile stress on the

Z-pin section, which is given in Eq. (B.2). The "lower" delamination surface, i.e. the surface of sub-laminate "C" in Fig. 14, located at $z = L^- - W$ = 2.8mm, while the "upper" delamination surface is at $z = L^- = 4\,\text{mm}$.

The model predicts the presence of two stress peaks, attained within the embedding sub-laminates and both close to the delamination surfaces. The stress peak near the upper delamination surface is the largest in magnitude, albeit the difference between the two stress maxima is small, i.e. about 1%. Note that the maximum stress has through in the unsupported region, i.e. for $L^- - W < z < L^-$; this occurs at the location where the bending moment acting on the Z-pin is zero, i.e. at the inflection point of the deformed Z-pin. There the stress is due only to the axial force and it is therefore constant on the Z-pin transversal section. This also demonstrates that the stress peaks shown in Fig. 14 are essentially due to the bending moment. In pure mode I, there will be no stress peaks, but a uniform stress region along the unsupported Z-pin length, i.e. $L^- - W < z < L^-$. In pure mode II, the stress peaks will be symmetric with respect to the delamination plane, with the zero bending moment inflection point located exactly above the latter.

For the stress distribution shown in Fig. 14, the Weibull's failure criterion in Eq. (31) predicts an average peak stress for failure $\overline{\sigma}_{\max}$ = 2887 MPa. Note that the latter value has been computed employing Eqs. (B.4), (B.6) and (B.7) and the calibrated Weibull's exponent from Tab. 3. As observed in Fig. 14, the peak tensile stress along the Z-pin axis exceeds $\overline{\sigma}_{\max}$ in a region located within the laminate, immediately below $\left(z = L^- - W\right)$ and above $\left(z = L^-\right)$ the delamination surfaces. These are the regions where the failure has the highest probability of occurring. In Fig. 15, the Weibull's failure probability from Eq. (30) using the stress field in Fig. 14 is plotted along the Z-pin axis.
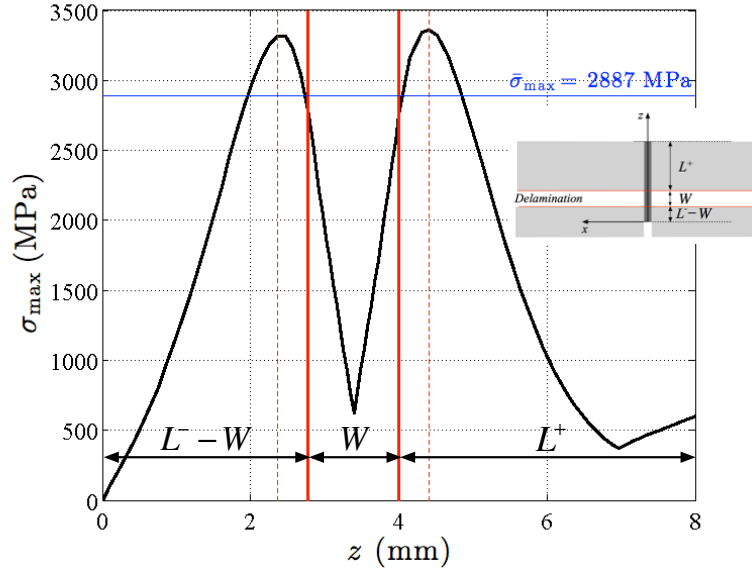
Fig. 14. Predicted maximum normal stress distribution at failure for $\phi = 0.550$.

Position of delamination surfaces in red continuous lines; the dashed red lines give the axial

locations of the stress peaks.

The cumulative probability of failure occurring in the Z-pin region below the lower delamination surface, i.e. for 2 mm $< z <$ $L^- - W = 2.8$ mm, is 48.2%. Similarly, the failure probability above the upper delamination surface, i.e. 4 mm $< z < 4.8$ mm, is 51.8%. Thus the Weibull's failure criterion predicts that failures will localise exactly where these are experimentally observed, i.e. within the laminate at a small distance from the delamination surfaces. This proves the robustness of the modelling approach proposed here.

6. Effects of cross-sectional shear

6.1 Shear stress distribution

During progressive pull out, the Z-pin is also subjected to a cross-sectional resultant shear force *T*, which is given by Eq. (A.8). From elementary beam theory, the resulting maximum

shear stress τ_{max} is attained at the centre of the Z-pin and it is given by 4/3 the applied shear force over the cross-sectional area, i.e.

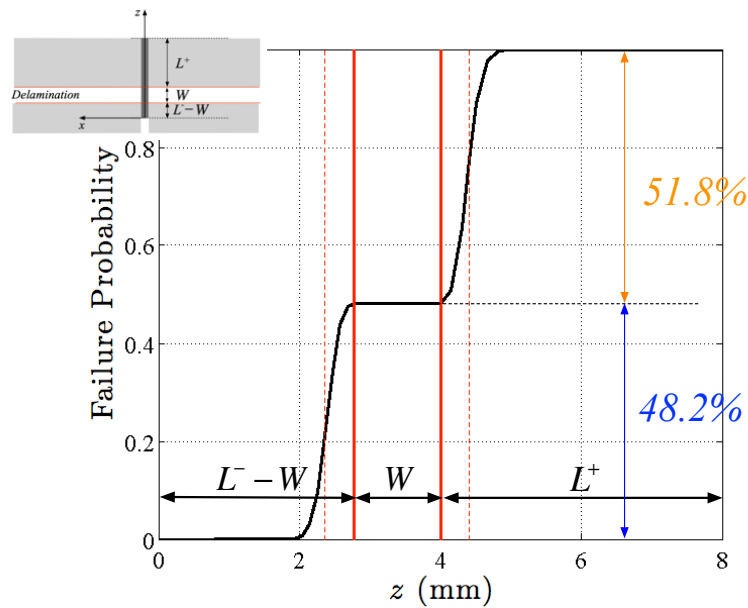$$|\tau_{max}| = \frac{16}{3\pi}\frac{T}{D^2} \tag{40}$$

Fig. 15. Failure probability along the Z-pin axis for the stress distribution in Fig. 14. Position of delamination surfaces in red continuous lines; the dashed red lines give the locations of the stress peaks.

A plot of the maximum shear stress from Eq. (40) and corresponding to the experimental failure load is shown in Fig. 16. One can immediately observe that the maximum shear stress is zero at the locations where the maximum normal stress is attained. The model predicts a maximum shear stress of 180 MPa in the unsupported segment of the Z-pin. Since the typical shear strength of fibre-reinforced plastics does not exceed 100 MPa [20], it has to be expected that longitudinal splitting of the through-thickness composite rod will occur, as already pointed out by the experimental tests in Ref. [8]. From the shear stress distribution shown in Fig. 16, it is reasonable to assume that the longitudinal splits will extend across the whole

unsupported length of the Z-pin and also partially within the sub-laminates, as shown in Fig. 17. Moreover, since the shear stress variations along the chords normal to the shearing direction are small, the split will span the whole chords, as shown in Fig. 17.
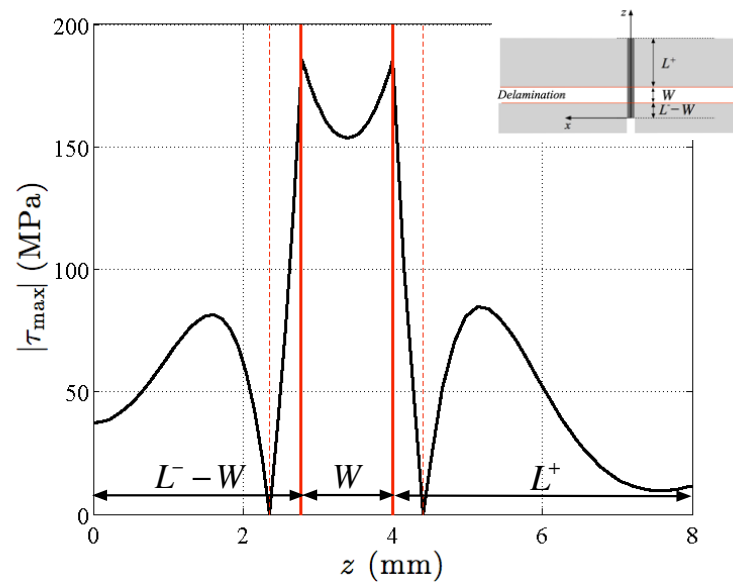

Fig. 16. Predicted maximum shear stress distribution at failure for $\phi = 0.550$.

Position of delamination surfaces in red continuous lines; the dashed red lines give the locations of the normal stress peaks.

6.2 Analysis of the Z-pin splitting

Fracture mechanics or a cohesive zone approaches would be required in order to investigate the actual split propagation once the initiation shear stress has been exceeded. Cui et al. [15] developed a 2D finite-element based modelling framework where potential splitting planes within the Z-pins were seeded with cohesive elements. They observed that the growth of the splits took place in mode II and it was also influenced by frictional stresses between the Z-pin strands separated by the splits. However it must be observed that the final results may depend on the pre-defined positions of the splits, as well as their overall number. Moreover the longitudinal split surfaces may not be exactly planar, thus some mechanical interlocking may

take place between the Z-pin strands. The propagation of the splits within the laminate is limited by the radial compressive stresses that are associated with the residual friction terms in Eq. (9), which are further by the lateral support of the elastic foundation. Clearly the main effect of the splits is to reduce the Z-pin bending stiffness, while the load carrying capability in terms of axial stress will be largely unaffected. In this respect the splitting does not constitute a critical failure mode, since the Z-pin will behave as a "bundle of bundles" [34] and the pull out can proceed until tensile fibre failure occurs.
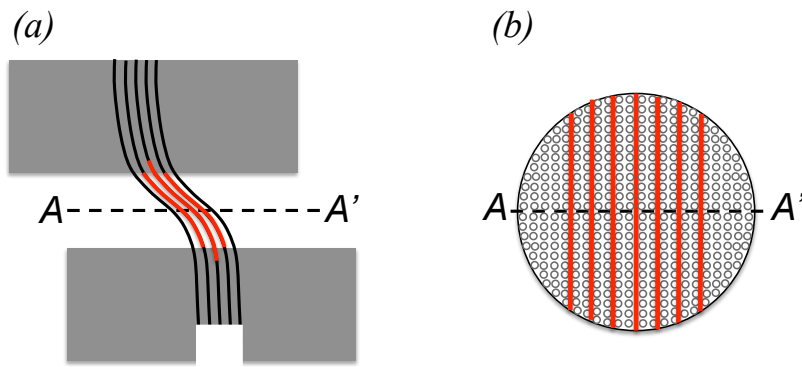

Fig. 17. Assumed configuration for the internal split in a composite Z-pin;

(a) side view; (b) cross-sectional view.

In order to explore the effect of internal splitting on the Z-pin response, we hereby introduce the simplifying hypothesis that the split propagation is limited to the unsupported region of the Z-pin. Let it be assumed that the deformed split segments have the lateral displacement and same curvature at each location within the unsupported segment, which are sufficient conditions for mode II splitting. By virtue of Eqs. (5) and (6), the equilibrium of the unsupported Z-pin segment is governed by the following differential equations

$$EI_s \frac{d^4u}{dz^4} - N \frac{d^2u}{dz^2} = 0 \tag{41}$$

$$\frac{dN}{dz} = -EI_s \frac{d^3u}{dz^3} \frac{d^2u}{dz^2} \tag{42}$$

where I_s is a reduced second moment of area given by

$$I_s = \frac{I}{\lambda} \tag{43}$$

In Eq. (43), I is the second moment of area for the pristine Z-pin, while λ is a damage variable, which accounts for the splitting of the Z-pin in multiple strands; I_s is given by the sum of the individual contributions to the second moment of area for each of the separated strands, calculated with respect to the neutral axis of each strand. For example, in the case of a single central split, the Z-pin is divided in two semi-circular halves; in this case, from elementary geometric considerations, one finds

$$\lambda = \frac{\pi}{\pi - \dfrac{64}{9\pi}} \cong 3.578 \tag{44}$$

Substituting into Eqs. (42) and (43) the normalised variables from Eq. (10) yields for the unsupported beam segment

$$y^{IV} - \lambda n y^{II} = 0 \tag{45}$$

and

$$n^{I} = -\frac{1}{\lambda}\left(\frac{D}{L}\right)^{2} y^{II} y^{III} \cong 0 \tag{46}$$

where the approximation holds by virtue of Eq. (15).

Therefore, in order to account for the internal splitting of the Z-pin, Eq. (45) is substituted into Eq. (22.a), leading to:

$$y^{IV} = \begin{cases} ny^{II} - 4\overline{\beta}^{4}y, & 0 \leq \xi \leq \alpha(1-d) \\[2mm] \lambda n y^{II}, & \alpha(1-d) \leq \xi \leq \alpha \\[2mm] ny^{II} - 4\overline{\beta}^{4}\left[y - \dfrac{\alpha\phi d}{\sqrt{1-\phi^{2}}}\left(\dfrac{L}{D}\right) \right], & \alpha \leq \xi \leq 1 \end{cases} \tag{47}$$

Note that, by virtue of Eq. (46), the differential equations for the normalised axial force in Eqs. (22.b) are valid also for the split Z-pin case.

The nonlinear differential system in Eqs. (22.b-25) and (47) is here solved following exactly the same solution strategy described in Sec. (5.1), using the calibrated parameters from Tab. 3. We consider here a worst-case scenario, whereby the splits are introduced in the entire unsupported length as soon as a shear stress of 100 MPa is reached within the Z-pin. This represents a limit case, but it would be extremely difficult to implement a realistic (either fracture mechanics of cohesive zone based) splitting initiation/propagation model within the semi-analytical framework introduced here. Three values of λ are considered, namely $\lambda = 3.578$ (single split case), $\lambda = 13$ (3 splits, uniformly spaced across the diameter) and $\lambda = 50$ (7 splits, uniformly spaced across the diameter).

The effect of the Z-pin splitting on the apparent fracture toughness is shown in Fig. 18. Up to a mode-mixity of 0.3, no longitudinal splitting occurs. For a mode-mixity between 0.3 and 0.4, the assumed splitting of the entire unsupported length leads to predicted premature failures of the Z-pins with respect to what observed in the experimental tests. The premature failures however yield an increase of the apparent fracture toughness, since they occur when the pull out is almost complete, so that the work associated with the frictional pull out is almost entirely added up to the fracture energy associated with the Z-pin rupture. In the mode-mixity range between 0.4 and 0.7, the apparent fracture toughness also increases with respect to the pristine Z-pin case and it tends to approach the average experimental value within the "transition" region (experimental datum at $\phi = 0.55$). However, the scatter in the experimental data is so large that it is not possible to conclude whether including the splits leads to an improvement of the model predictions. Notably, the presence of splits makes a negligible difference for $\phi > 0.7$. This is due to the fact that, when approaching mode II, $G^*(\phi)$ is dominated by the fracture toughness of the Z-pin tensile fibre failure.
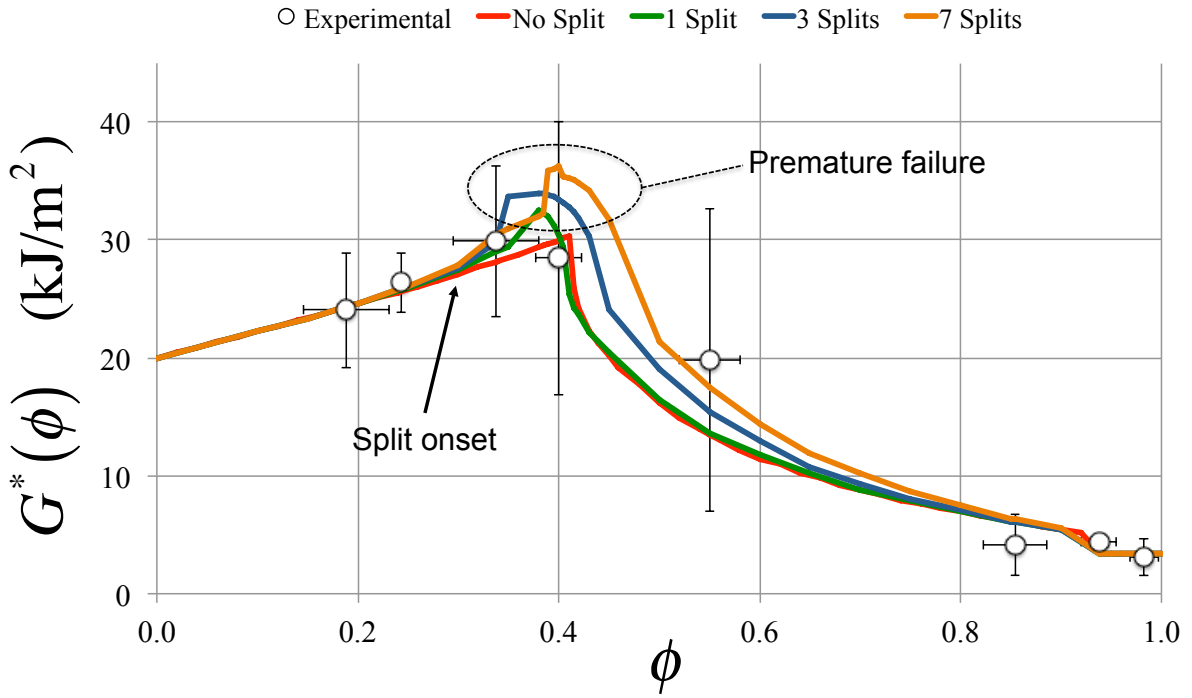
Fig. 18. Effect of longitudinal splits on apparent fracture toughness
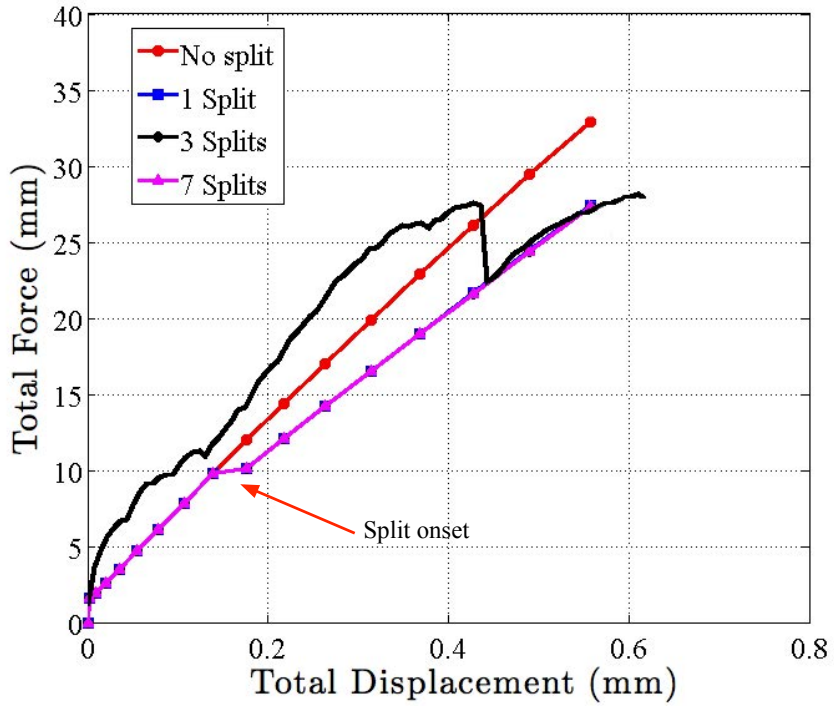

Fig. 19. Effect of longitudinal splits on the mode II dominated response ($\phi = 0.983$).

Average experimental load-displacement curve in black.

The results in Fig. 18 show that the instantaneous propagation of the splits in the whole unsupported region is a too severe assumption for $\phi < 0.4$. This suggests that, even if multiple splits initiate, the energy release rate available for their growth is relatively limited. Of course this scenario should be investigated in a fracture mechanics or a cohesive zone framework in order to provide a definitive answer.

Fig. 19 shows the predicted mode II response for the split Z-pin. The onset of longitudinal splitting occurs for very small delamination sliding displacements and applied loads, respectively 0.13 mm and 10 N. This causes a sudden drop of stiffness with respect to the pristine Z-pin case, but, most interestingly, the predicted responses are insensitive to the number of splits, since the associated curves in Fig. 19 are almost coincident. The displacement to failure is also unaffected by the number of splits, whereas the failure load drops by almost 20%. However, the failure load is still within the scatter bands shown in Fig. 7.b, while, as remarked above, the corresponding apparent fracture toughness is unaffected by the presence of the splits.

7. Conclusions

A new micro-mechanical model for describing the delamination bridging action exerted by Z-pins has been presented and validated. The model is based on describing Z-pins as Euler-Bernoulli beams embedded in an elastic foundation and subjected to small but finite rotations of the transversal cross-section. The response of Z-pins is obtained by solving a system of non-linear differential equations, which govern the Z-pin equilibrium for a set of prescribed pull out and sliding displacements. The model is valid for fibrous and brittle Z-pins, whose failure is described by the Weibull's criterion.

The apparent fracture toughness of a Z-pin reinforced composite is directly related to the energy dissipated by the frictional pull out of the Z-pins. Considering the specific case of

quasi-isotropic laminates, it has been demonstrated that the apparent fracture toughness provided by Z-pin insertion increases with the mode-mixity, until a critical value of the latter is reached. This is due to the fact that the residual friction experienced by the Z-pin is initially by Coulomb friction in a mixed-mode regime. The friction enhancement increases the axial tension and bending that the Z-pin must support during pull out, leading to failure of the through-thickness reinforcement once a characteristic critical mode-mixity is exceeded. The critical mode-mixity for the Z-pin/laminate arrangement considered here is $\phi = 0.400$. The transition from complete pull out to failure causes a progressive reduction of the apparent fracture toughness. In pure mode II, the apparent fracture toughness of a through-thickness reinforced laminate is entirely due to the fracture toughness associated with the tensile fibre failure of the Z-pins.

There exists a significant amount of scatter in both the apparent toughness versus mode-mixity data and the Z-pin load versus displacement curves. The scatter increases significantly in the transition region from complete pull out to failure, even if the misalignment angles associated with the Z-pin insertion are taken into account when calculating the actual mode-mixity for each of the coupons tested. The post-insertion residual curvature of Z-pins may play a significant role in this respect, since it can induce residual axial stresses in the Z-pin that may promote or delay failure at a given value of the mode-mixity.

The geometrically non-linear Euler-Bernoulli beam model presented in this paper requires calibration of 6 parameters in total. The identification of these parameters has been carried out via a genetic algorithm, considering the load-displacement curves for the Z-pins tested in a mode I and a mode II dominated regime, together with the overall trend of the apparent toughness with respect to the actual mode-mixity (i.e. considering the Z-pin misalignment angles for each coupon tested).

Employing the 6 parameters mentioned above, the modelling approach proposed here yielded results that are in excellent agreement with the mean experimental load-displacement curves and the average apparent fracture toughness over the whole mode-mixity range. Bridging force-opening/sliding displacement relationships (Eq. 36) have been defined, which are suitable for implementation in interface element formulations for the FE analysis of Z-pin reinforced composite structures. Similarly, the apparent toughness trend obtained from the model can be employed for modelling the Z-pin bridging via cohesive zone models. The implementation of the model presented in this paper to the definition of suitable interface element formulations and cohesive zone models will be addressed in future work.

Acknowledgements

References

[1] Allegri G., and Zhang X., Delamination/Debond Growth in Z-fibre Reinforced Composite T-Joints: a Finite Element Simulation. In: Proceedings of the ECCM-11 Conference, Rhodes, Greece, May 31-June 3, 2004.

[2] Allegri G., Zhang X., On the Delamination Suppression in Structural joints by Z-fiber Pinning. Composites Part A: Applied Science and Manufacturing; 28(4), pp. 1107-15, 2007.

[3] Bianchi F., Zhang. X., Predicting Mode-II Delamination Suppression in Z-pinned Laminates. Composites Science and Technology; 72(8), pp. 924-32, 2012.

[4] Bianchi F., Koh T.M., Zhang X., Partridge I.K., Mouritz, A.P., Finite Element Modelling of Z-pinned Composite T-joints. Composites Science and Technology; 73, pp.48-56, 2012.

[5] Bullock, R. E., Strength Ratios of Composite Materials in Flexure and in Tension, Journal of Composite Materials; 8, pp. 200-206, 1974.

[6] Cartié D.D.R., Effect of Z-Fibres^{TM} on the Delamination Behaviour of Carbon Fibre/ Epoxy Laminates. PhD Thesis, Cranfield University, Chapter 7, pp. 31-45, 2000.

[7] Cartié D.D.R., and Partridge I.K., A finite element tool for parametric studies of delamination in Z-pinned laminates. In: Proceedings of the DFC6 Conference, Manchester, UK, 4-5 April 2001.

[8] Cartié D.D.R., Cox B.N., and Fleck N.A., Mechanisms of Crack Bridging by Composite and Metallic rods. Composites Part A: Applied Science and Manufacturing; 35(11), pp. 1325-36, 2004.

[9] Cartié D.D.R., Dell'Anno G., Poulin E., Partridge, I.K., 3D Reinforcement of Stiffener-to-Skin T-joints by Z-pinning and Tufting. Engineering Fracture Mechanics; 73(16), pp. 2532-2540, 2006.

[10] Cartié D.D.R., Troulis M., and Partridge I.K., Delamination of Z-pinned Carbon Fibre Reinforced Laminates. Composites Science and Technology; 66(6), pp. 855-861, 2006.

[11] Chang P., Mouritz A.P., and Cox B.N., Properties and Failure Mechanisms of Z-pinned Laminates in Monotonic and Cyclic tension. Composites Part A: Applied Science and Manufacturing; 37(10), pp. 1501-13, 2006.

[12] Cox B.N., Massabò, R., and Rugg K.L., The science and engineering of delamination suppression. In: Proceedings of the DFC6 Conference, Manchester, UK, 4-5 April 2001.

[13] Cox B.N., and Sridhar N., A Traction Law for Inclined Tows Bridging Mixed-Mode Cracks. Mechanics of Composite Materials and Structures; 9, pp. 299-331, 2002.

[14] Cox B.N., Snubbing Effects in the Pullout of a Fibrous Rod from a Laminate. Mechanics of Advanced Materials and Structures; 12, pp. 85-98, 2005.

[15] Cui H., Lia Y., Koussiosb S., Zub L., Beukersb A., Bridging Micromechanisms of Z-pin in Mixed Mode Delamination, Composite Structures; 93(11), pp. 2685-95, 2011.

[16] Fang Z., Liu L., Gu. A., Wang X., and Guo Z., Improved Microhardness and Microtribological Properties of Bismaleimide Nanocomposites Obtained by Enhancing Interfacial Interaction through Carbon Nanotube Functionalisation, Polymer Advanced Technologies; 20, pp. 849-856, 2009.

[17] Farley G.L., and Dickinson L.C., Mechanical Response of Composite Material with Through-the-Thickness Reinforcement. In: NASA Conference Publication, Issue 3176, 1992.

[18] Freitas G., Magee C., Dardzinski P., and Fusco T., Fiber Insertion Process for Improved Damage Tolerance in Aircraft Laminates. Journal of Advanced Materials; 25(24), pp. 36-43, 1994.

[19] Grassi M., and Zhang X., Finite Element Analyses of Mode I Interlaminar Delamination in Z-fibre Reinforced Composite Laminates. Composites Science and Technology; 63(12), pp. 1815-1832, 2003.

[20] Hallett S.R., Green B.G, Jiang W.G., and Wisnom M.R., An Experimental and Numerical Investigation into the Damage Mechanisms in Notched Composites, Composites Part A:, Applied Science and Manufacturing; 40(5), pp. 613-624, 2009.

[21] Koh T.M., Feih S. and Mouritz A.P., Experimental Determination of the Structural Properties and Strengthening Mechanisms of Z-pinned Composite T-joints. Composite Structures;93, pp. 2269-76, 2011.

[22] Massabò R., and Cox B.N., Concepts for Bridged Mode II Delamination Cracks. Journal of the Mechanics and Physics of Solids; 47(6), pp. 1265-1300, 1999.

[23] Massabò R., and Cox B.N., Unusual Characteristics of Mixed Mode Delamination Fracture in the Presence of Large Scale Bridging. Mechanics of Composite Materials and Structures; 8(1), pp. 61-80, 2001.

[24] Mouritz A. P., Review of Z-pinned Composite Laminates, Composites Part A: Applied Science and Manufacturing; 38(12), pp. 2383-97, 2007.

[25] Mouritz A.P., Chang P. and Isa M.D., Z-pin Composites: Aerospace Structural Design Considerations, Journal of Aerospace Engineering; 24, pp. 425-432, 2011.

[26] Partridge I.K., and Cartié D.D.R., Delamination Resistant Laminates by Z-Fiber[TM] Pinning. Part I: Manufacture and Fracture Performance. Composites Part A: Applied Science and Manufacturing; 36(1), pp. 55-64, 2005.

[27] Pinho S.T, Robinson P., Iannucci L., Fracture Toughness of the Tensile and Compressive Fibre Failure Modes in Laminated Composites, Composites Science and Technology; 66(13), pp. 2069-2079, 2006.

[28] Ratcliffe J.G., and O' Brien T.K., Discrete spring model for predicting delamination growth in Z-fiber reinforced DCB specimens. NASA/TM-2004-213019, May 2004.

[29] Rosen, B.W. and Zweben, C.H., Tensile Failure Criteria for Fiber Composite Materials, NASA CR-2057, 1972.

[30] Rugg K.L., Cox B.N., Ward K.E., and Sherrick G.O., Damage Mechanisms for Angled Through-Thickness Rod Reinforcement in Carbon-Epoxy Laminates. Composites Part A: Applied Science and Manufacturing; 29(12), 1998.

[31] Rugg K.L., Cox B.N., and Massabò R., Mixed-Mode Delamination of Polymer Composite Laminates Reinforced Through the Thickness by Z-fibers. Composites Part A: Applied Science and Manufacturing; 33, pp. 177-90, 2002.

[32] Schön, J., Coefficient of Friction and Wear of a Carbon Fiber Epoxy Matrix Composite, Wear; 257 (3-4), pp. 395-407, 2004.

[33] Timoshenko, S.P., On the Correction Factor for Shear of the Differential Equation for Transverse Vibrations of Bars of Uniform Cross-Section, Philosophical Magazine, 41, pp. 744-746, 1921.

[34] Wisnom, M.R, The Effect of Specimen Size on the Bending Strength of Unidirectional Carbon Fibre-Epoxy, Composite Structures; 18 (1), pp. 47-63, 1991.

[35] Yan W., Liu H.Y., and Mai Y.W., Numerical Study on the Mode I delamination Toughness of Z-pinned Laminates. Composite Science and Technology; 63, pp.1481-93, 2003.

[36] Yan W., Liu H.Y., and Mai Y.W., Mode II delamination toughness of Z-pinned laminates. Composite Science and Technology; 64, pp. 1937-45, 2004.

[37] Yasaee M., Lander J.K, Allegri G., Hallett S.R, Experimental Characterisation of Mixed Mode Traction-Displacement Relationships for a Single Carbon Composite Z-pin, Composites Science and Technology, http://dx.doi.org/10.1016/j.compscitech.2014.02.001 2014.

[38] Zhang, X., Hounslow L., Grassi M., Improvement of Low-Velocity Impact and Compression-after-impact Performance by Z-fibre Pinning, Composites Science and Technology, 66(15), pp. 2785-94, 2006.

[39] D3039/D3039M-08 Standard Test Method for Tensile Properties of Polymer Matrix Composite Materials, ASTM International, 10.1520/D3039_D3039M-08, 2008.

[40] Torayca® T300 Data Sheet. Available online at: http://www.toraycfa.com/pdfs/T300DataSheet.pdf ; last retrieved on February 11th 2013.

Appendixes

A. Equilibrium equations

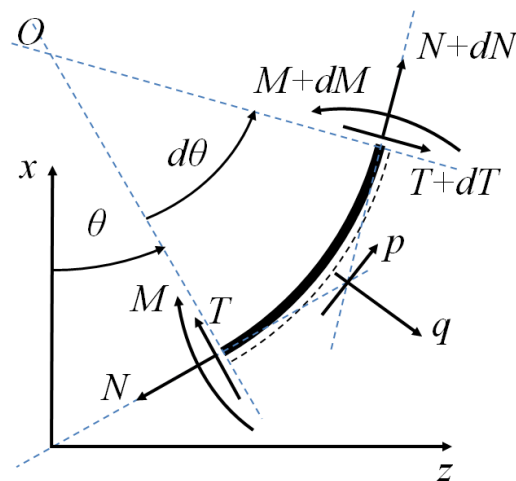
Fig. A.1. Equilibrium of forces and moments for the deformed beam segment.

An infinitesimal deformed beam segment is considered in Fig. A.1. N and T denote respectively the normal and shear force resultants on the beam section. M represents the local resulting bending moment. Distributed tangential p and normal q forces act on the beam lateral surface. The undeformed beam axis lays on the z Cartesian direction shown in Fig. A.1; θ is the angle between the local tangent to the beam deformed axis and the z coordinate axis. The equilibrium equations for the deformed beam segment in terms of cross-sectional resultants are the following

$$\frac{d}{ds}(N\cos\theta + T\sin\theta) + p\cos\theta + q\sin\theta = 0 \tag{A.1}$$
$$\frac{d}{ds}(N\sin\theta - T\cos\theta) + p\sin\theta - q\cos\theta = 0$$
$$\frac{dM}{ds} = T$$

For small axis rotations, i.e. $\theta \ll 1$, Eq. (A.1) can be linearized as follows

$$\frac{d}{dz}(N + T\theta) + p + q\theta = 0 \tag{A.2}$$
$$\frac{d}{dz}(N\theta - T) + p\theta - q = 0$$
$$\frac{dM}{dz} = T$$

Expanding the derivatives in first of Eq. (A.2), solving with respect to $\dfrac{dN}{dz}$ and multiplying both sides by θ yields

$$\theta\frac{dN}{dz} = -T\frac{1}{2}\frac{d\theta^2}{dz} - \theta^2\frac{dT}{dz} - p\theta - q\theta^2 \cong -p\theta \tag{A.3}$$

since $\theta \ll 1$ as assumed above. Expanding the derivatives in the second of Eq. (A.2), solving with respect to $\dfrac{dT}{dz}$ and making use of Eq. (A.3) leads to

$$\frac{dT}{dz} = N\frac{d\theta}{dz} - q \tag{A.4}$$

Thus, differentiating the third of Eq. (A.2) with respect to *z* and combining the result with Eq. (A.4) yields

$$\frac{d^2M}{dz^2} = N\frac{d\theta}{dz} - q \tag{A.5}$$

Considering an Euler-Bernoulli beam, whose cross-sections stay normal to the deformed axis, the following relation holds between the rotation angle θ and the beam transversal displacement in Cartesian coordinates *u*

$$\theta = \frac{du}{dz} \tag{A.6}$$

Assuming that the beam material is linear elastic, Eq. (A.6) implies that the following relation holds between the cross-sectional resultant bending moment *M* and the curvature of the beam axis

$$M = EI\frac{d^2u}{dz^2} \tag{A.7}$$

where *E* is th Young's modulus and *I* the cross-sectional second moment of area.

Substituting Eq. (A.7) into the third of Eq. (A.2) leads to the relation between the beam transversal displacement *u* and the cross-sectional shear resultant

$$T = EI\frac{d^3u}{dz^3} \tag{A.8}$$

Combining Eq. (A.4), (A.6) and Eq. (A.8) leads to the following equation governing the beam transversal displacement

$$EI\frac{d^4u}{dz^4} - N\frac{d^2u}{dz^2} + q = 0 \tag{A.9}$$

Solving the first of Eq. (A.2) with respect to $\frac{dN}{dz}$, making use of Eq. (A.4) and neglecting the terms in θ^2 yields

$$\frac{dN}{dz} = -T\frac{d\theta}{dz} - p \tag{A.10}$$

Substituting Eq. (A.6) and (A.8) into Eq. (A.10) leads to

$$\frac{dN}{dz} = -EI\frac{d^3u}{dz^3}\frac{d^2u}{dz^2} - p \tag{A.11}$$

Eq. (A.11) governs the beam axial equilibrium. By virtue of Eqs. (A.2), (A.6) and (A.8), the local projections of the axial and shear forces on the z and x axes for small rotations are given by

$$Z = N + EI\frac{d^3u}{dz^3}\frac{du}{dz} \tag{A.12}$$
$$X = N\frac{du}{dz} - EI\frac{d^3u}{dz^3}$$

B. Weibull's failure criterion

B.1 Strength scaling

A beam having a constant circular cross section with diameter D is subjected to combined tension and bending along its longitudinal axis z. A representative section of the beam is sketched in Fig. B.1. The axial force is denoted as $N(z)$ and the bending moment is $M(z)$.
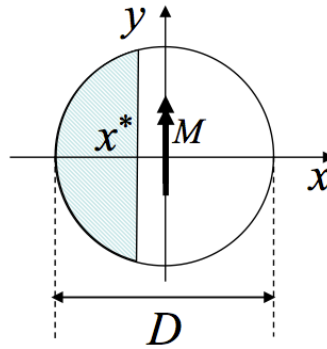

Fig. B.1. Cross section; the shaded area is assumed to be in tension.

Let the following characteristic ratio of tension to bending be introduced

$$\omega(z) = \frac{N(z)D}{M(z)} \tag{B.1}$$

Let $\sigma_{max}(z)$ be the peak tensile stress on the section, which is attained for $x = -\dfrac{D}{2}$. With the help of some basic beam theory, it is straightforward to show that the axial stress distribution in the beam is given by

$$\sigma(x,z) = \sigma_{max}(z) \frac{\omega(z) - 16\dfrac{x}{D}}{\omega(z) + 8} \tag{B.2}$$

The volume integral that appears in Eq. (32) can be calculated as follows

$$\int_V \left[\frac{\sigma(x,y,z)}{\sigma_s}\right]^m dV = \int_0^L \left[\frac{\sigma_{max}(z)}{\sigma_s}\right]^m \frac{1}{[\omega(z)+8]^m} \left\{ \int_{A^*} \left[\omega(z) - \frac{16x}{D}\right]^m dx\,dy \right\} dz = \tag{B.3}$$

$$= \int_0^L \left[\frac{\sigma_{max}(z)}{\sigma_s}\right]^m \frac{1}{[\omega(z)+8]^m} \left\{ \int_{-\frac{D}{2}}^{x^*(z)} \int_{-\sqrt{\frac{D^2}{4}-x^2}}^{\sqrt{\frac{D^2}{4}-x^2}} \left[\omega(z) - \frac{16x}{D}\right]^m dx\,dy \right\} dz =$$

$$= \int_0^L \left[\frac{\sigma_{max}(z)}{\sigma_s}\right]^m \frac{2}{[\omega(z)+8]^m} \left\{ \int_{-\frac{D}{2}}^{x^*(z)} \left[\omega(z) - \frac{16x}{D}\right]^m \sqrt{\frac{D^2}{4} - x^2}\, dx \right\} dz$$

where x^* represent the bound of the cross-sectional sector subjected to tension, as shown in Fig. B.1.

Defining

$$G(z) = \frac{2}{[\omega(z)+8]^m} \left\{ \int_{-\frac{D}{2}}^{x^*(z)} \left[\omega(z) - \frac{16x}{D}\right]^m \sqrt{\frac{D^2}{4} - x^2}\, dx \right\} \tag{B.4}$$

and applying the mean value theorem, the integral in Eq. (B.3) is equivalently expressed as

$$\int_V \left[\frac{\sigma(x,y,z)}{\sigma_s}\right]^m dV = \left[\frac{\overline{\sigma}_{max}}{\sigma_s}\right]^m V_{eff} \tag{B.5}$$

where V_{eff} represents the beam effective volume

$$V_{eff} = \int_0^L G(z)\,dz \tag{B.6}$$

In Eq. (B.5) $\overline{\sigma}_{max}$ is the average peak tensile stress along the beam axis, which is given by

$$\overline{\sigma}_{\max} = \left[\frac{\int_0^L \sigma_{\max}^m (z) G(z) dz}{V_{eff}} \right]^{\frac{1}{m}}$$

<div align="right">(B.7)</div>

Thus the Weibull's failure probability given in Eq. (31) can be expressed simply as

$$P_F = 1 - e^{-\left(\frac{\overline{\sigma}_{\max}}{\sigma_s}\right)^m V_{eff}}$$

<div align="right">(B.8)</div>

Let us consider a second body/load configuration, i.e. a cylindrical bar having arbitrary cross-section and subjected only to constant tension along its longitudinal axis. The Weibull's failure probability in this case is expressed as [33]

$$P_F = 1 - e^{-\left(\frac{X}{\sigma_s}\right)^m V_0}$$

<div align="right">(B.9)</div>

where V_0 is the volume of the bar and X the applied tensile stress. The strengths at constant failure probability for the two configurations will therefore be related by the following identity

$$X_T^m V_0 = \overline{\sigma}_{\max}^m V_{eff}$$

<div align="right">(B.10)</div>

Assuming that X_T represents the average tensile strength associated with the volume V_0, solving Eq. (B.10) with respect to $\overline{\sigma}_{\max}$ yields the failure criterion in Eq. (32).

B.2 Further remarks on the effective volume

As a special case, one can consider a circular bar subjected to constant axial force and bending along its length, i.e. $\omega(z) = \omega$. Assuming that L_0 is the length of the bar, the associated geometrical volume is $V = \frac{\pi D^2 L_0}{4}$. From Eqs. (B.4) and (B.6), the following expression of the ratio of the effective volume to the geometrical volume is sought for $\omega < 8$

$$\frac{V_{eff}}{V} = \frac{2}{\pi} \frac{1}{[\omega+8]^m} \int_{-1}^{\frac{\omega}{8}} [\omega - 8x']^m \sqrt{1-x'^2}\, dx' \qquad \text{(B.11)}$$

For $\omega \geq 8$ one has

$$\frac{V_{eff}}{V} = \frac{2}{\pi} \frac{1}{[\omega+8]^m} \int_{-1}^{1} [\omega - 8x']^m \sqrt{1-x'^2}\, dx' \qquad \text{(B.12)}$$

It is worth observing that in pure tension, i.e. $\omega \to \infty$, Eq. (B.12) yields

$$\lim_{\omega \to \infty} \frac{V_{eff}}{V} = \frac{2}{\pi} \int_{-1}^{1} \sqrt{1-x'^2}\, dx' = 1 \qquad \text{(B.13)}$$

so the effective and geometrical volumes are the same, as it must be expected. On the other hand when pure bending is applied, i.e. $\omega = 0$, one finds

$$\frac{V_{eff}}{V} = \frac{2}{\pi} \int_{0}^{1} t^m \sqrt{1-t^2}\, dt = \frac{1}{\pi} \beta \left[\frac{3}{2}, \frac{1}{2}(m+1) \right] \qquad \text{(B.14)}$$

where β is the Euler Beta function.

A plot of the ratio between the effective and geometrical volumes as a function of Weibull's modulus for a subset of ω values is presented in Fig. B.2.
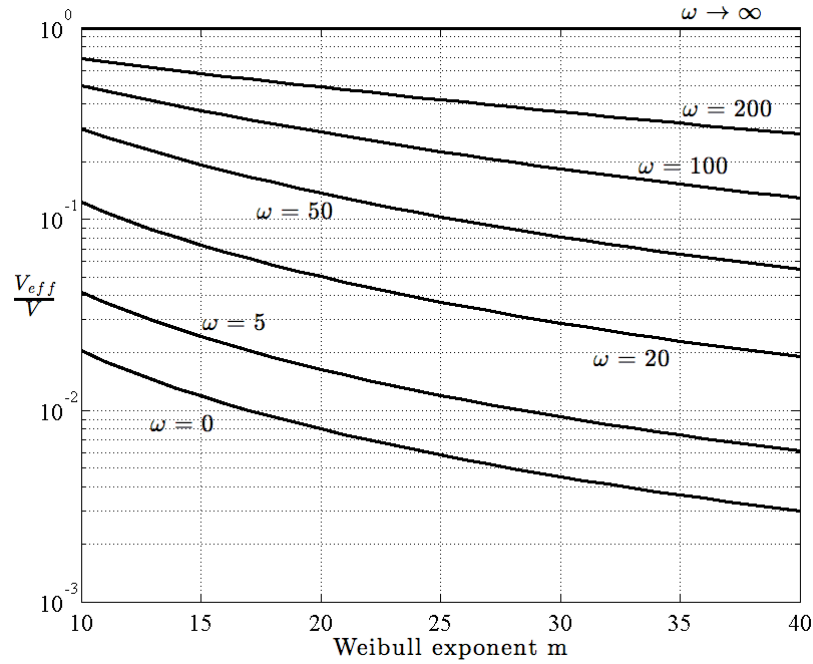

Fig. B.2. Ratio of the effective volume to the geometrical volume.

C. Timoshenko's Beam in Winkler Foundation

The Timoshneko's beam equation in presence of an axial force N and a distributed transversal load q reads

$$EI\frac{d^4u}{dz^4} - N\frac{d^2u}{dz^2} = -q + \frac{EI}{\kappa AG_{LT}}\frac{d^2q}{dz^2} \tag{C.1}$$

From Eq. (C.1), switching to the normalised variables in Eq. (10) and considering the expression of the foundation forces from Eqs. (7), for the lower embedded segment one has:

$$y^{IV} - ny^{II} = -4\overline{\beta}^4\left(y - \frac{EI}{\kappa G_{LT}AL^2}y^{II}\right) \tag{C.2}$$

Eq. (C.2) proves the Timoshenko's model reverts to the Euler-Bernoulli theory if the condition stated in Eq. (28) holds even if the beam is embedded into an elastic foundation. It is straightforward to prove that the same holds true for the upper embedded segment of the Z-pin.